Strain Imaging and Vascular Elasticity

BY

JEROME J MAI
B.S. (University of California, Berkeley) 1998

THESIS

Submitted in partial satisfaction of the requirements for the degree of

MASTER OF SCIENCE

in

Biomedical Engineering

in the

OFFICE OF GRADUATE STUDIES

of the

UNIVERSITY OF CALIFORNIA

DAVIS

Approved:

_____

Michael F. Insana

_____

Gary E. Ford

_____

Craig K. Abbey

Committee in Charge

2002

TABLE OF CONTENTS

LIST OF FIGURES

LIST OF TABLE

ABSTRACT

Soft tissue strain imaging (elastography) and vascular elasticity are two topics that have spawned much research in the past years.

Strain imaging is an ultrasound method used to detect elastic inhomogeneities in soft tissues, in vivo. Many lesions become stiff with advancing disease and yet are not detectable with conventional imaging methods, including ultrasound, CT, MRI. Though not yet widely adopted clinically, strain imaging techniques have been used in vivo to detect abnormal growths in breasts, prostates, and kidneys, since many diseased tissues such as tumors exhibit increased stiffness. Rooted in the ultrasonic tissue motion measurements, this relatively young field started gaining interest in the early 90s [Ophir et al 1991]. Various improvements and modifications of the underlying signal processing techniques have been implemented throughout the years. Multi-compression [Skovoroda et al 1994], subsample time delay [Céspedes et al 1995], temporal-stretching [Varghese et al 1996], and 2-D companding [Chaturvedi et al. 1998a] are just some of the ways to improve accuracy while reducing noise in strain images. It has been shown that strain imaging techniques are highly sensitive, accurate, and able to sense displacements on the scale of micrometers [Insana et al. 2000]. This thesis extends the strain imaging techniques to be able to study vascular elasticity non-invasively using commercial imaging systems.

High blood pressure and cardiac problems are often associated with increased stiffness in the vascular system. The elastic properties of vasculature have thus been of interest for many decades. Peterson et al. carried out studies on arteries in 1960, and the findings are still used today. The measurement of vascular elasticity relies on an accurate estimation of the vessel size and its variation in response to changing internal pressure. Many ultrasonic techniques are already available now for measurement of vessel wall motion. These techniques include locating vessel walls based on echo intensity [Arndt et al. 1968], identification of the vascular lumen using Doppler flow information [Hoeks et al. 1985, Reneman et al. 1986], tracking of vessel wall using zero-crossing techniques [Imura et al. 1986], auto segmentation of the borders based on graph search [Sonka et al. 1998], cross-correlation of the 1D RF signal [Hoeks et al. 1993], etc. Along with the different techniques, a multitude of definitions is used to quantify the arteries' dimensional response to changes in pressure [Lehmann 1998]. My work has been to understand how vascular strain imaging can contribute to the assessment of vascular health, in vivo.

Soft tissue and vascular elasticity measurements share similar diagnostic goals yet each has its own set of terminology and challenges. Here I present my work on bridging these two areas of research. The first chapter is based on a published journal paper covering a qualitative study of non-invasive strain imaging for describing internal deformations. The second chapter reports results from a series of quantitative studies that extend the first study using vessel-mimicking phantoms. Each chapter can be read independently; the first emphasizes strain imaging and the second emphasizes

displacement estimates. Many terms and definitions in the two areas are discussed and associated here. Observation and experimentation are carried out in vivo and on various phantoms that I developed. Though the results do not suggest a simple answer, they indeed open the door to future research topics.

CHAPTER 1

Strain Imaging of Internal Deformation

Abstract

A tissue-like gelatin elasticity-flow phantom was examined to develop ultrasonic strain imaging for the detection of internal pulsatile deformations. The same imaging technique was then applied *in vivo* to monitor deformation in tissues surrounding the normal brachial artery. The results suggest that vascular strain patterns resulting from biological stimuli are very different from those generated using externally applied stress fields, and are directly related to pressure variations within the vessel. These data suggest a potential role for strain imaging in measuring the relative pressure or vascular elasticity locally and non-invasively.

Keywords: brachial artery, elasticity, phantoms, pulsatile flow, strain imaging, ultrasound, vascular imaging

Accepted in Ultrasound in Medicine and Biology August 2002

1.1. INTRODUCTION

Several techniques use signals from imaging systems to form diagnostic images that describe the spatial and temporal distributions of tissue elasticity, *in vivo*. Ultrasonic applications alone span a broad range from tumor detection [Garra et al. 1997] to characterization of vascular plaques [de Korte et al. 2000] and assessment of vascular health [Hoeks et al. 1999] to the study of skeletal muscle contraction [Levinson et al. 1995] to the assessment of fetal lung maturity [Adler et al. 1990]. Today, the most common approaches measure soft tissue strain produced by an external stress stimulus, either statically applied by the imaging transducer or a vascular balloon, or dynamically applied by introducing shear waves into the body. However the study of ultrasonic elasticity began with Dickinson and Hill [1982], Wilson and Robinson [1982], and Tristam et al. [1986] who measured deformations of tissues, including tumors, from natural internal stress stimuli such as cardiac contractions. These are dynamic analyses that have been limited to single A-line or M-mode analyses of tissue because of the technology available at the time. Each describes tissue kinetics but with little or no spatial resolution.

The technology exists today for recording the complex envelope of echo samples for extended fields of view at video frame rates using laboratory and commercial systems. Thus it is now possible to apply wide-band signal processing analysis to measure displacements along the beam axis as small as 5^{o} of phase (3 μm at 7 MHz) or with a spatial resolution comparable to B-mode imaging [Insana et al. 2000]. We are

exploring this opportunity to image blood vessels, specifically, to visualize viscoelastic deformations surrounding vessels during cardiac pulse propagation. Potential applications of this approach include local measurements of relative arterial pressure or vascular elasticity, plaque characterization, and the development of noninvasive methods for studying the relationship between blood-flow dynamics and tissue elasticity.

This report describes our initial investigations using a tissue-like elasticity-flow phantom with flow channels to which we applied static or pulsatile hydraulic pressures. The intent is to assess the sensitivity of displacement and strain measurements in a relatively simple tissue-like media. Finally, *in vivo* measurements in a brachial artery of a normal volunteer are presented.

1.2. MATERIALS AND METHODS

1.2.1. Materials

A well-known hydro-gel material formed the bulk of the ultrasonic elasticity-flow phantom constructed for this study [Hall et al. 1997; Zagzebski and Madsen 1995]. The material composition by mass was 83.93% distilled water, 7.72% n-propanol, 5.04% animal-hide gelatin powder (275 bloom), 0.05% formaldehyde, and 3.26% graphite powder. These ingredients provided a durable viscoelastic material with temporally stable acoustic and elastic properties in the range of many soft tissues. The molten mixture was poured into a 10 x 8 x 7.4 cm^3 acrylic container and slowly rotated while congealing to keep the graphite particles suspended. Nine 1.3-mm-diameter acrylic rods

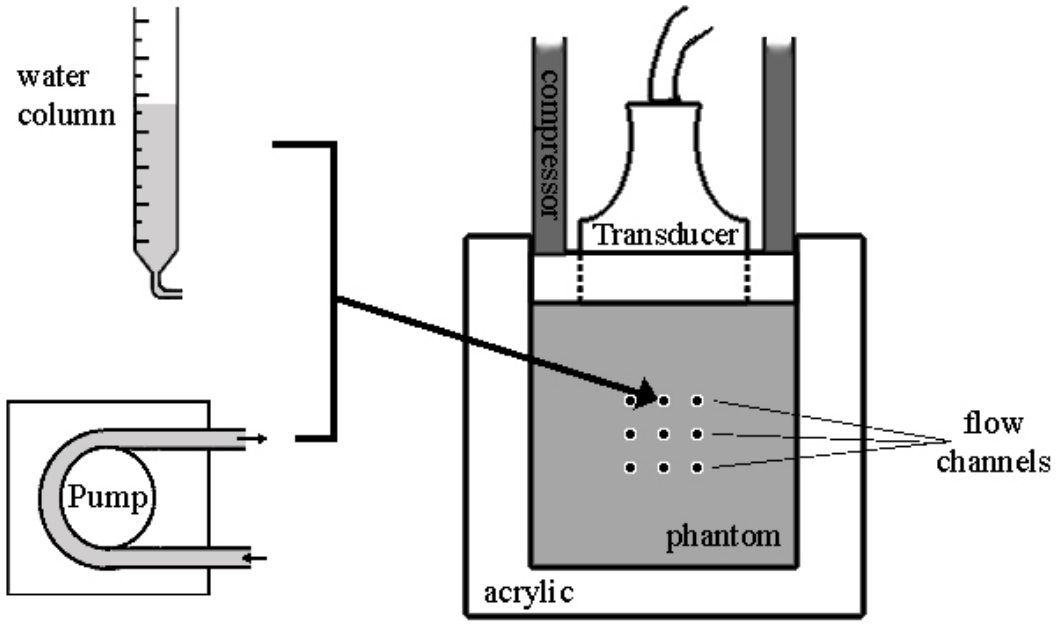

Fig. 1.1. Setup of the elasticity-flow phantom and scanning apparatus. Channel flow is directed into the plane. A water column of adjustable height can be connected to the flow channel while sealing the other end to create internal hydrostatic pressure. A peristaltic pump can be connected to both ends of a channel to create hydrodynamic pressures.

were positioned centrally in the rectangular container, each parallel to the others and separated 10 mm on center. They were removed after the gel congealed to provide wall-less fluid channels in the gel block (Fig. 1.1). Previous phantom designs include rigid flow channels inappropriate for this study [Rickey et al. 1995] or elastic walls that are made of highly attenuating material. Stiff plastic tubes were securely inserted 5 mm into channel as inlets and outlets to connect the phantom to flow sources and sinks. Fluid flowed through channels under gravitational feed for steady flow and under peristaltic pump feed for pulsed flow. The fluid was a weak suspension of cornstarch (less than 0.4% by mass) in water to provide some ultrasonic scattering. The cornstarch particles in

solution can remain suspended for a longer period of time if the solution was heated to boil and then cooled to room temperature. The acoustic properties of the fluid were not measured.

1.2.2. Acoustic Measurements

One extra sample of the graphite-gelatin material of 2.54-cm thickness was prepared during phantom construction for measurements of acoustic properties. Sound speed and attenuation coefficient were measured at 21^{o}C using the narrow-band, through-transmission substitution technique of Madsen et al. [1982]. The attenuation coefficient at 7.5 MHz was 2.92 dB/cm and the speed of sound was 1567 m/s. Attenuation in this material is known to increase approximately linearly with frequency [Madsen 1978]. The attenuation measurement was calibrated using a castor oil sample [Madsen 1982], with error between expected and measured values within 10%.

1.2.3. Viscoelastic Measurements

We also measured the elastic modulus of the graphite-gelatin material using an indentation test on the surface of the elasticity-flow phantom [Kargel 2001]. A computer-controlled linear positioner, with 0.1-mm positional precision, and a flat-ended cylindrical indenter (radius a = 2.5 mm) provided the compression to the sample. A digital electronic balance with negligible movement measured the load with a precision of 0.01g. The apparatus was controlled under Labview to record force (F) and indentation depth (w) in real time. Measurements were obtained from least squares estimates of the data during the compressional phase for indentations between 0.0 and

0.25 mm, which is the range of the imaging experiments described below. Elastic modulus was calculated using the formula $E = F(1-\upsilon^2)/2aw\kappa$, assuming Poisson's ratio υ = 0.498 for nearly incompressible material and κ = 1 for large sample thickness [Zhang et al. 1997]. The elastic modulus estimate was 10.7 kPa.

1.2.4. Ultrasonic Echo Recording

To acquire echo data, we used a Siemens Elegra system with a 7.5 MHz linear array (7.5L40) transmitting 7.2 MHz broadband pulses. A single transmit focal zone was centered on the target. Viewing the real-time B-mode image display and adjusting the depth-gain compensation manually to give constant echo amplitude with depth over the region of interest, we acquired digitized echo signals from system memory. Echo frames containing 312 data segments (0.12 mm transducer pitch) of in-phase/quadrature (I/Q) time series were recorded at 15 frames per second (fps). A total of seventy-three echo frames were recorded from a region 51.3 mm deep and 38 mm wide. Radio-frequency (RF) signals were digitized at 36 Msamples/s, mixed to form I/Q data, downsampled by 2.5 for electronic transfer, and then upsampled by 4 before processing. We formed strain images from echo data with an effective (fast-time) RF data density of 57.6 Msamples/s and a bandwidth of 18 MHz. The 15-fps (slow-time) sampling rate provided about four cycles of pulsed flow data at 60 fluid pulse cycles/min. I/Q data were transferred via a network connection for offline processing on a Pentium III computer.

1.2.5. Strain Image Formation

Strain images are formed from correlation-based displacement estimates. Local displacements are determined from pairs of RF data frames acquired for the same region in the object but at two times representing different stages of deformation. The Chaturvedi algorithm [1998a, 1998b] was used for all displacement estimates and strain images reported in this study. The algorithm was originally developed for imaging strain resulting from external compression (Appendix A), but is appropriate for imaging internal deformation from pulsed flow since displacements are usually small. From segmentation of the channel margins detected in B-mode images reconstructed from the high-density I/Q data, we were able to quantitatively determine that the maximum radial displacement for pulsatile flow measured along the sound beam was approximately 0.1 mm.

With this algorithm, we compute local displacements within the scan plane of the deformed object from 2-D correlation lags determined at three spatial scales. First, the coarsest estimates of displacement are used to measure and compensate for the overall (average) displacement and strain applied to one frame with respect to another. The process of warping echo data in a frame to compensate for the average physical deformation is known as global companding. Second, displacements measured at an intermediate-size spatial resolution (the 2-D data kernel was 1 x 1 mm^2) are recorded and used to warp the echo fields via a local companding process. Finally, displacements are measured at the highest spatial resolution by 1-D correlation of twice companded echo frames. Three-point quadratic interpolation is also used in the correlation step to estimate fractional displacement. Displacement measurements from one stage of estimation

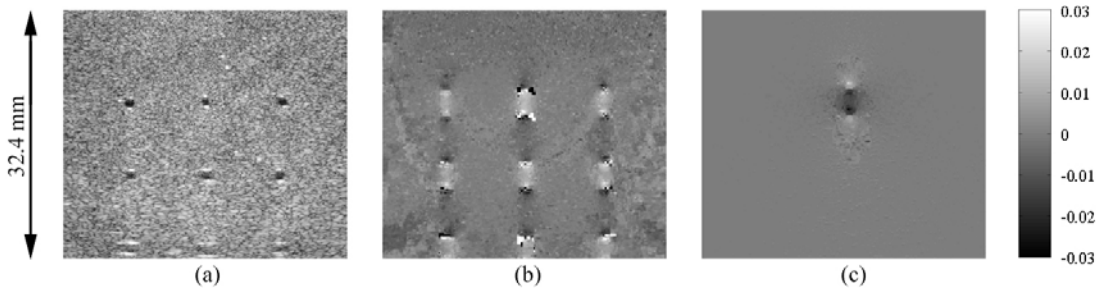

Fig. 1.2. **(a)** B-mode image of the elasticity-flow phantom. **(b)** Strain image of the elasticity-flow in the same region of interest, generated with 2% external axial compression. **(c)** A typical strain image of the internal deformation, with only one channel under internal stimulus.

improve the condition of the data for estimation at higher resolution [Insana et al. 2000]. Companding is a 2-D analogue of the 1-D "temporal stretching" technique implemented by others [Céspedes and Ophir 1993; Céspedes et al. 1993; Varghese et al. 1996a, 1996b]. Finally, components of displacement along the ultrasonic beam axis at each stage are summed and filtered by a two-sample FIR differentiator to form strain images. Axial strain pixel size is determined by parameters set at the final stage of displacement estimations. However, each stage of the estimation process and the echo impulse response of the instrumentation determine spatial resolution of the strain image.

For internal deformation imaging, global companding is not used for confined phantoms but is applied when scanning *in vivo*. Although the average strain expected in an echo frame recorded during pulsed flow is zero, global companding compensates for in-plane transducer motion at the skin surface that commonly occurs during live scanning.

1.3. RESULTS

1.3.1. Phantom Imaging with External Stimulus

The elasticity-flow phantom was mounted in an acrylic fixture, placed in distilled water, and scanned along a central plane with a linear array transducer (Fig. 1.1). In this phase of the study, and contrary to that shown in Fig. 1.1, channels were not connected to pressure sources (water column or pump) and boundaries were confined only to prevent out-of-plane motion; the phantom was free to move within the scan plane. The pre-compression B-mode image and corresponding strain image with 2% applied compressive strain are shown in Figs. 1.2a and 1.2b, respectively. Channels were filled with distilled water that moved freely when the phantom was deformed. As expected, strains around the channels are larger than in the background (bright pixels in Fig. 1.2b indicate soft areas). By extending the length of the correlation window to minimize strain noise, we introduced shape distortions: channels appear much larger in the vertical dimension than their actual 1.3-mm-diameter size. Also, decorrelation errors are observed above and below each channel, particularly in the bottom row where defocusing reduces the echo signal-to-noise ratio. Decorrelation errors (high-contrast black and white pixels) are seen where strain gradients are large or shear strains are significant, which is often the case near region boundaries with sharp elastic modulus contrast. Decorrelation errors can be mitigated in some situations by adjusting the correlation window size, as described in the Discussion section below.

1.3.2. Phantom Imaging with Internal Stimulus

The apparatus illustrated in Fig. 1.1 was used for imaging local deformation from static or pulsatile pressures applied to the top-center flow channel. In this phase of the study, no external stress was applied and each exterior surface was rigidly confined in the acrylic mold. In the first experiment, hydrodynamic pressures were produced with a peristaltic pump (Gilson Minipuls 2) that generated pulsatile flow within a closed loop in the top-center channel. The pressure pulse rate was roughly 1 pulse/s with a time average flow of 0.114 ml/s. The measured time-pressure curve is shown in Fig. 1.4a. In the second experiment, hydrostatic pressures were generated in the same channel by connecting one side to a water column and blocking flow in the other. In either case, the image plane was located near the center of the phantom, perpendicular to the channel axis. Tygon tubing that was much stiffer than the phantom material joined the pump or water column to the phantom channel. Consequently, nearly all of the deformation from the pressure pulse occurred inside the phantom channel. The pressure variation inside the channel was also measured at the time of image acquisition with a medical pressure transducer system (Medex LogiCal pressure transducer, Puritan-Bennett Co. PB240 patient monitor).

1.3.3. Pulsatile Pressure as Internal Stimulus

Deformation varies with time for pulsatile flow. Therefore one of the echo frames must be selected as a reference to compute the sequence of strain images. The choice of reference frame is arbitrary yet it dramatically influences strain contrast. To simplify interpretation of the strain patterns, we chose the reference frame at the time when the channel pressure was lowest (smallest channel diameter) out of the 16 frames recorded

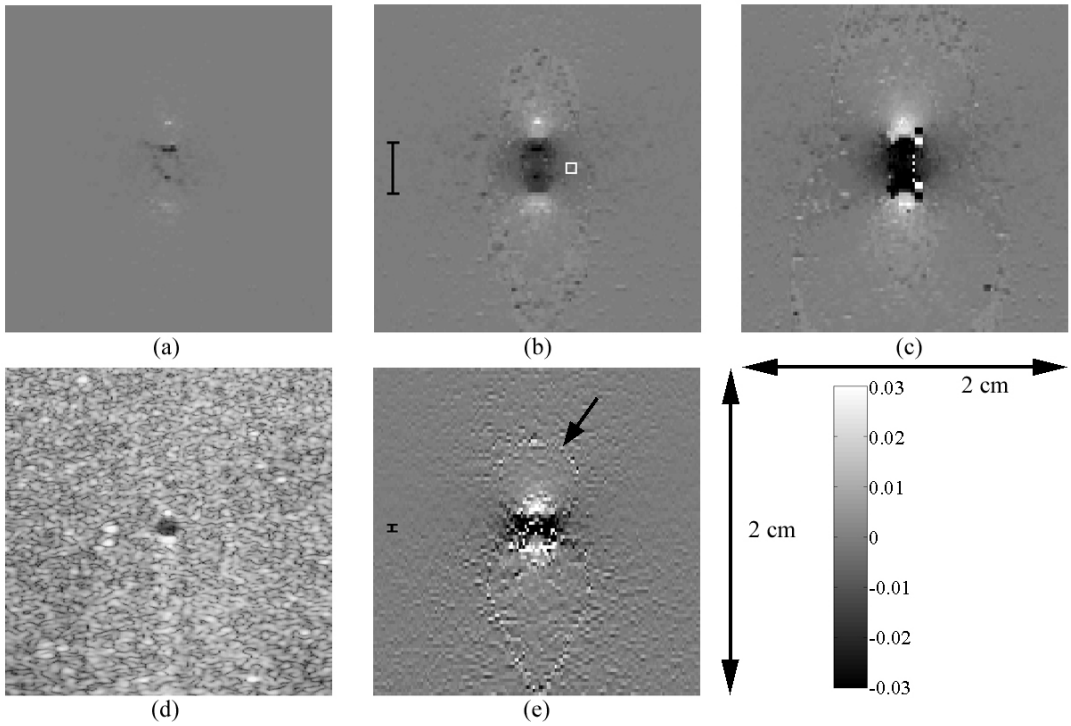

Fig. 1.3. **(a-c)** are strain images of a region surrounding a channel under pulsatile flow at different stages of one pulse cycle. They are processed with a correlation window of 3.33 mm, size represented by the "I" in (b). **(d)** is the same region in B-mode. **(e)** is the same strain image as (b), but processed with a correlation window of 0.42 mm, represented by the "I" in the image. The arrow in (e) points at the emphasized dipole pattern. The white box in (b) defines the region over which the average strain was estimated for Fig. 1.4b. The grayscale bar indicates the strain range (unitless).

for one complete cycle. Consequently, by definition, all movement in the scan plane was directed radially outward from the channel, and the time-varying strains were compressive.

Fig. 1.2c shows a typical strain image of the phantom with the top-center channel under internal stimulus. Though the same region of interest is displayed, strain patterns in Fig. 1.2c are very different from those of the external stimulus in Fig. 1.2b. First, the local nature of the stress field means that only deformed structures near the channel

appear in the image. Second, the deformation pattern is distorted vertically because we selected a long, narrow correlation window to reduce the strain noise caused by echo noise. Third, some regions appear bright, indicating compressive strain, while others appear dark, indicating an apparent tensile strain. Although we know that the strains are compressive and radially directed, the linear array transducer senses displacements only along the axis of the sound beam. Strain patterns in Figs. 1.2b and 1.2c are both determined by the elastic modulus of the medium and the applied stress field. Unlike that in Fig. 1.2b, the stress field in the images of Fig. 1.2c is time varying, acts locally, and is radially directed. Strain values in Fig. 1.2c exhibit a dipolar spatial pattern because the measurements depend strongly on the orientation of the sound beam with respect to the movement. The appearance of strain patterns seen in Fig. 1.2c is explained in terms of the beam geometry in the Discussion section.

Figs. 1.3a-c, separated by 1/3 s between each image, show the strain images at three different stages in one pulse cycle, all displayed in the same region of interest as the zoomed-in B-mode image in Fig. 1.3d. Fig. 1.3a is near the start of the pulse when the channel was least expanded, so most of the image is gray (zero strain). As the channel pressure increases, the expanded channel deforms the surrounding medium, thus providing strain contrast. In Fig. 1.3c, which was near the peak of the pulse cycle, decorrelation effects can be seen around the channel. Both Fig. 1.3b and 1.3e were generated with the same echo frame pair, but 1.3b was processed with a correlation window of 3.33 mm, while 1.3e was done with 0.42 mm. Though the strain patterns in Fig. 1.3e give a more realistic description of the channel geometry, the decorrelation

noise has significantly increased. Also the aforementioned dipolar pattern becomes more obvious in Fig. 1.3e (arrow).

To study how the internal stimulus affects the strain images, we took advantage of the simple phantom geometry to find a relationship between channel pressure and local phantom strain. We were able to adopt a 2-D elasticity model [Volterra and Gaines 1971] that predicts displacements around a wall-less channel in a elastic medium along lines radial from the center of the channel. Similar equations have also been used to describe a finite-thickness cylindrical phantom imaged with intravascular ultrasonography [de Korte et al. 1997]. The displacement $u_r(r,t)$ is a function of radial distance *r*, time *t*, and is dependent on the channel pressure $P(t)$:

$$u_r(r,t) = \frac{(1+\upsilon)D^2}{4rE} P(t), \qquad \text{for} \quad r \geq D/2. \tag{1.1}$$

E is the elastic modulus of the gelatin material surround the channel, υ is the Poisson ratio of the gelatin, and *D* is the reference frame channel diameter. The corresponding radial strain in the object is

$$\varepsilon_r(r,t) = -\frac{du_r(r,t)}{dr} = \frac{(1+\upsilon)D^2}{4r^2E} P(t) \ . \tag{1.2}$$

The convention for strain imaging is to define compressive strain as a positive quantity. Eqs. 1.1 and 1.2 predict that radial displacements and strains are proportional to pressure inside the channel. To test this prediction, we first plotted the pressure profile within one cycle inside the channel by averaging over several cycles (Fig. 1.4a). We then calculated for one pulse cycle the averaged strain magnitude in a rectangular region (0.7

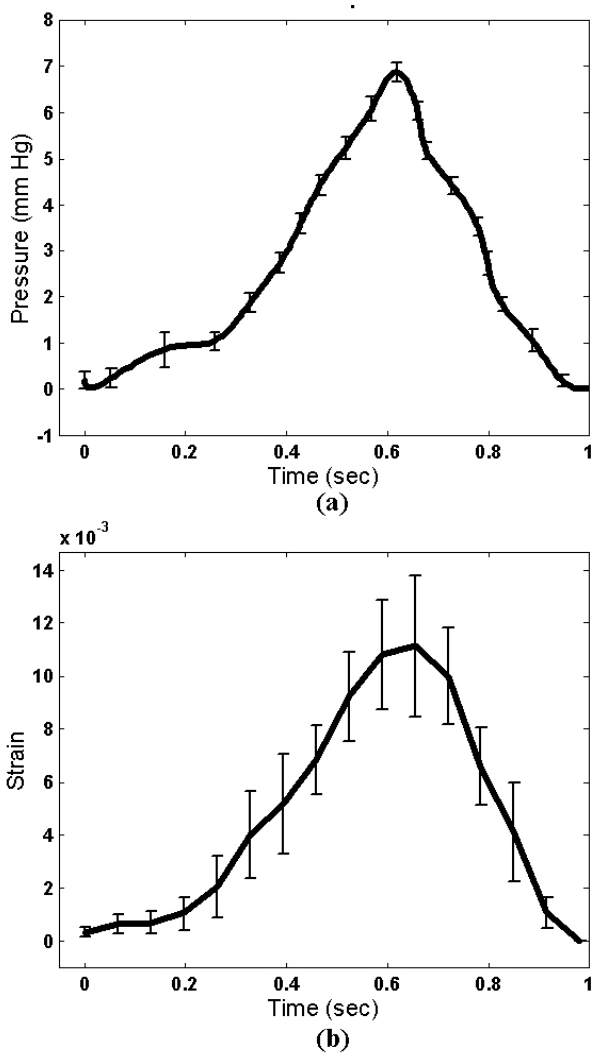

Fig. 1.4. **(a)** The pressure profile of one cycle of the pulsatile flow is generated and plotted by averaging several cycles. **(b)** The average strain magnitude in boxed region in Fig. 1.3b is plotted for the entire pulse cycle. Error bars indicate one standard deviation of the mean.

x 0.8 mm^2, boxed region in Fig. 1.3b) that is 1.8 mm to the right of the channel center. Results are plotted in Fig. 1.4b. This region, processed with a 3.33-mm correlation window, was picked for its low level of decorrelation. Though a phase lag might exist between the two plots in Fig. 1.4, we can easily see the similarity between them and that

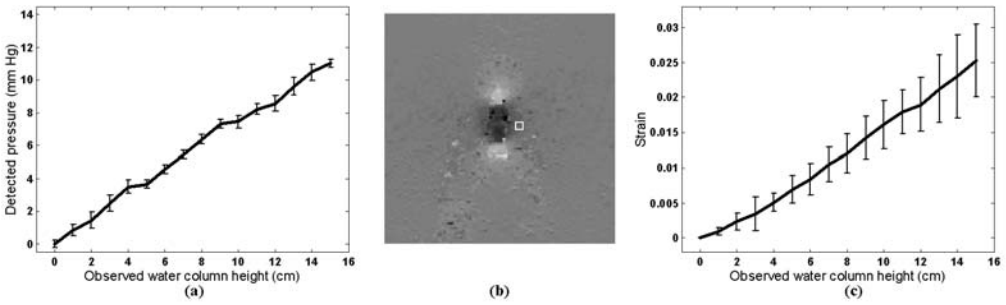

Fig. 1.5. **(a)** The measured pressure variation inside a channel is plotted against the observed water column height for the hydrostatic pressure experiment. Error bars indicate one standard deviation of the mean over 5000 samples in 5 s. **(b)** A typical strain image of the static internal deformation. **(c)** The average strain magnitude in boxed region in (b) is plotted as a function of water column height, with error bars indicating one standard deviation of the mean.

the strain is directly related to the amount of pressure inside the channel. The maximum strain in the pulse cycle was reached with a relative pressure of 6.8-mmHg.

1.3.4. Hydrostatic Pressure as Internal Stimulus

A strain-pressure calibration curve was also measured for the hydrostatic pressure inside the phantom generated by the water column. Under controlled static pressure, the relationship between pressure and strain can be studied without being affected by variables like flow and the phase lag in pulse propagation. The “zero pressure” water height was established by letting water move freely through the unsealed ends of the channel when the phantom was completely submerged in water. The echo frame acquired at this “zero pressure” was used as reference frame for generating strain images. After sealing off the outlet of the channel, water was then added to the column at 1-cm increments to a maximum height of 15 cm, which converts to a pressure of 11.07-mmHg. Since the reading of the water height was more error-prone, the pressure variation was

also monitored with a pressure transducer and averaged over five seconds at each step (Fig. 1.5a). Echo data were taken and a strain image was processed at each pressure increment. The averaged strain magnitude in the aforementioned region (boxed region in Fig. 1.5b) was calculated as well for the 16 pressure levels. The averaged strain magnitude (Fig. 1.5c) increased linearly with pressure between 1-11 mmHg. Comparing Figs. 1.4 and 1.5, we see that the proportionality between pressure and strain holds for both static and dynamic stresses.

1.3.5. In Vivo Brachial Artery Imaging

Brachial artery was chosen for *in vivo* testing because systemic blood pressure is conventionally measured there on the upper arm with a sphygmomanometer. Also, this location is acoustically accessible and provides reasonable echo signal strength and imaging resolution. The orientation of the arm and the location of the artery can make full acoustic contact difficult. We obtained reproducible sets of echo data by mounting the transducer at an oblique angle with a rotary device and a linear positioner (Fig. 1.6). The arm rested on the transducer surface that is flush mounted to a flat plate. Abundant coupling gel and the weight of the arm pressing the skin against the transducer ensured full acoustic contact. The elbow was raised slightly above shoulder height to ensure no pooling of blood in the veins in the nearby region. Subjects held their breath during data acquisition to minimize external movement. We acquired echo data from several consecutive cardiac cycles at 15 fps. The frame with the smallest arterial diameter, corresponding to end diastole, is the reference frame for generating strain images. The

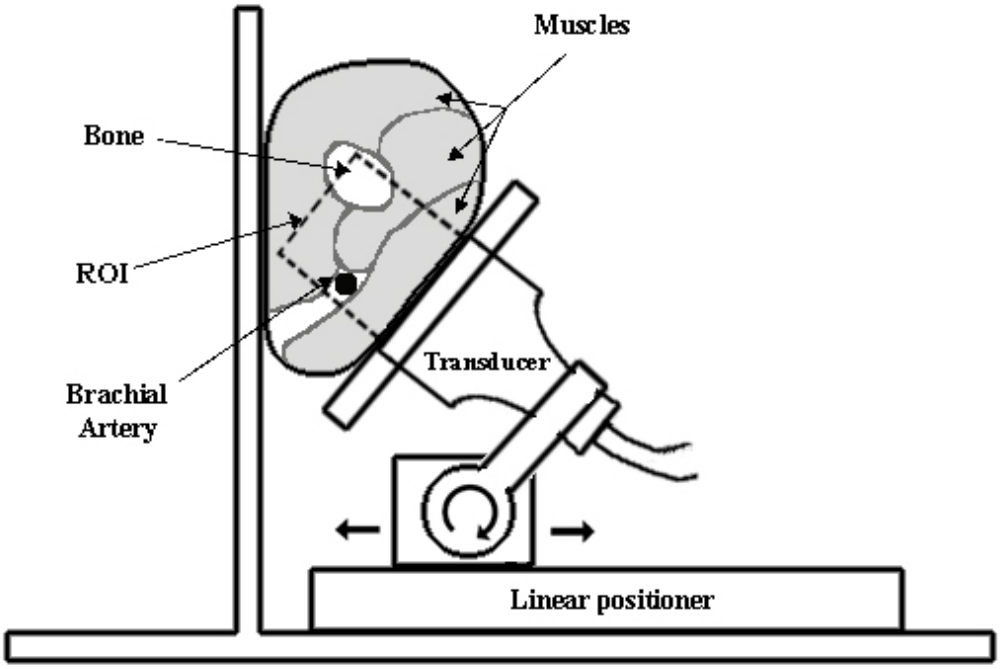

Fig. 1.6. Upper right arm rests on the slanted transducer-embedded plate while the echo data of the cross section is acquired. The upper arm, with its cross-sectional anatomy shown in the figure, is positioned horizontally in this view. The positioning device and rotary unit accommodate arms of different sizes. For full acoustic contact, the brachial artery sometimes can not be centered in the ROI due to the arm's curved surface.

data recorded of the right arm of a healthy 25-y.o. male volunteer with a blood pressure reading of 135/80 mmHg are displayed in this study.

Fig. 1.7a shows a B-mode image of the upper arm region containing the brachial artery at end diastole. The brachial artery is the dark circular object in the mid-right region of the B-mode image; it is approximately 3 mm in diameter at end diastole. Three muscle groups separated by fascia surround this artery: biceps, brachialis, and triceps. Smaller arteries, veins, and nerves covered by fascia also reside in the regions next to the brachial artery. We generated 46 strain images over three cardiac cycles. Fig. 1.7b-e are

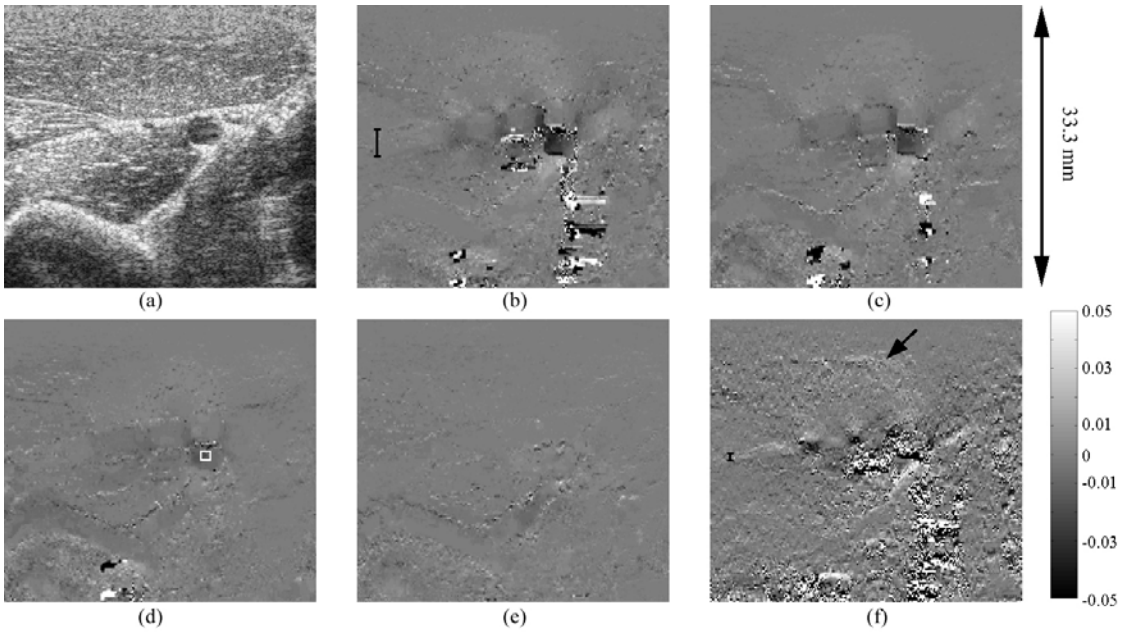

Fig. 1.7. **(a)** is the B-mode image of a region around the brachial artery. **(b-e)** display the strain images of the brachial artery from peak systole to near end diastole, processed with a 3.33 mm-long correlation window represented by "I" in (b). The white box in (d) defines the region over which the average strain was estimated for Fig. 1.8a. **(f)** is the same strain image as (b), but processed with a 0.83 mm-long correlation window. The arrow in (f) points at a combined asymmetric dipole pattern from the brachial artery and two other pulsing vessels to the left of brachial artery.

four strain images from peak systole to near end diastole separated in time by ¼ s and generated with a 3.33-mm-long correlation window. The artery is most distended at peak systole and then gradually returns to minimal size. Vascular pulsatility in Fig. 1.7 produces strain patterns similar to those of the pulsing phantom channel in Fig. 1.3, although it is clear that the heterogeneity of surrounding tissues in the arm have a strong affect on strain images. For example, the humerus bone, which appears in the lower left corner of the B-mode image, seems to act as a rigid boundary that limits deformation of the tissue surrounding the vessels. The dipolar strain pattern is apparent above the vessels but not below. Other artifacts also exist in these images. Three smaller internal

deformation strain patterns, which may be caused by smaller vessels, are also visible to the left of the brachial artery. These effects are much clearer with short correlation windows (0.83 mm, Fig. 1.7f), though the compromise between spatial resolution and noise that occurs by varying the window length is apparent. Strain imaging appears capable of detecting deformation asymmetry such as that caused by the proximity of the humerus bone, and its high sensitivity to small strain variations suggests the possibility of detecting regional arterial elasticity changes caused by the formation of plaques and calcification.

We measured one mean regional strain magnitude in a 0.6 x 1.0 mm^2 region (boxed region in Fig. 1.7d) at the brachial artery for each strain image in our time series. These values are plotted versus time for three cardiac cycles in Fig. 1.8a. Though the smoothness of this plot is limited by the frame rate at which echo data were collected, the plot clearly depicts the essential characteristics of brachial arterial pressure profile seen in Fig. 1.8b [Remington and Wood 1956; Salans et al. 1951]. Comparing these curves, we observe that there is a close relationship between the variations in cardiac pressure and those from the resultant strain. Notice that the region selected for computing the averaged strain magnitude is inside the lumen of the artery. Here strain estimates are based on the movement of the vessel wall and its small reflection in the lumen, and processed with a relatively large correlation window (see Discussion). Also, if we increase the pressure of the transducer against the arm, we may find larger fluctuations in strain surrounding the brachial artery during each cardiac cycle. This response is expected – external force increases vascular resistance in the measurement region by

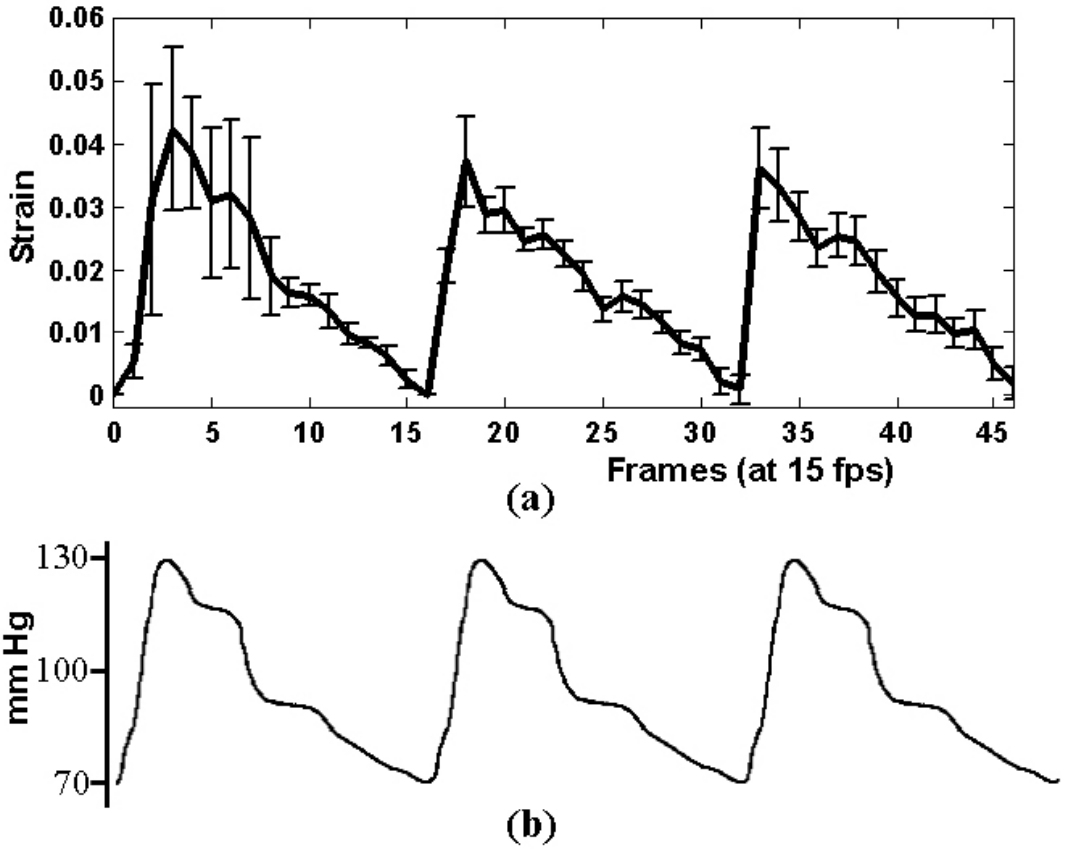

Fig. 1.8. **(a)** The average strain magnitude in the boxed region in Fig 1.7d is plotted for three cardiac cycles, with error bars illustrating one standard deviation of the mean. **(b)** The shape of a normal pressure wave at brachial artery is drawn for three cardiac cycles. The resemblance between these plots illustrates a relationship between the strain observed and the pressure variation inside the artery.

adding pressure in the surrounding tissue to reduce the vessel cross sectional area. It is important to maintain a consistent and minimal pressure between the transducer and skin surfaces to avoid disturbing the natural deformation of tissues surrounding arteries during the cardiac cycle.

1.4. DISCUSSION

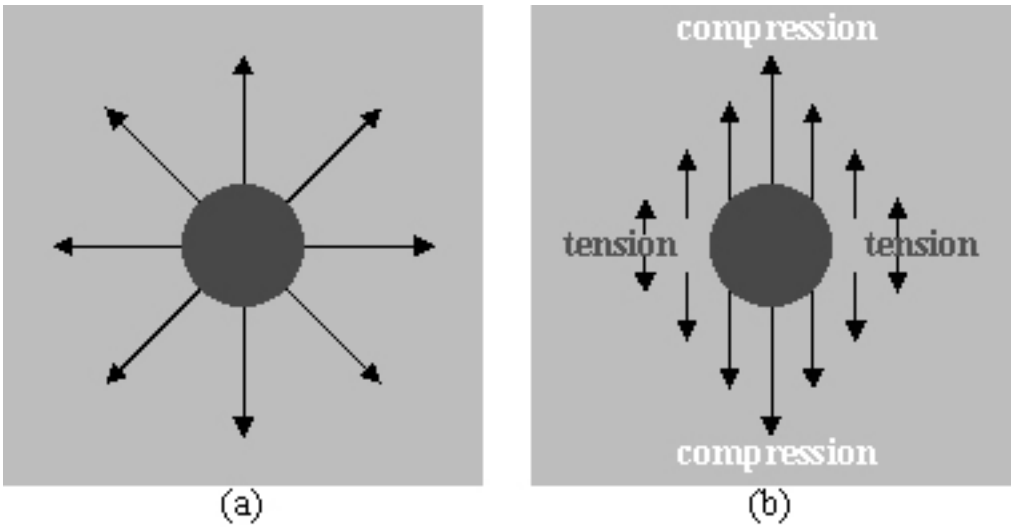

Fig. 1.9. The dark gray circle represents a fluid flow channel in the phantom, whereas the light gray background is the gelatin. **(a)** The arrows indicate the direction of forces acted upon the regions around the channel as the channel expands radially. **(b)** Our strain algorithms sense the axial strain caused by the axial components of the forces shown by the arrows. This results in compression above and below the channel, while tension in regions lateral to the channel.

1.4.1. Interpretation of Strain Patterns from Pulsatile Pressure

Strain patterns near a pulsing vessel are very different from those formed with external compression. The pressure pulse in the channel expands the walls radially outward (Fig. 1.9a) thus compressing the surrounding regions. Pulse-echo ultrasound can only sense these very tiny movements if they occur along the direction of wave propagation (Fig. 1.9b). Consequently the echo data records only a component of the displacement vector, that in the direction of the beam axis, *z*. $u_z(r,t)$ is proportional to $u_r(r,t)$. For uniform radial displacement, we can assume

$$u_z(r,\theta,t) = u_r(r,t)\cos\theta, \quad \text{for} \quad r \geq D/2. \tag{1.3}$$

The angle θ defines the direction of motion in the imaging plane with respect to *z* (see Eq. 1.1). As shown in Fig. 1.9b, the axial strain, i.e., the strain component along the

beam axis, is compressive (bright pixels) in regions above and below the vessel, near $\theta = 0, \pi$. However, the axial strain occurring in regions lateral to the vessel, near $\theta = \pm\pi/2$, is tensile (dark pixels). The radial projection of displacement onto the *z*-axis produces a dipole pattern in the strain image. The dipole pattern is nearly symmetric in the phantom because radial expansion is almost uniform over θ. The weight of the phantom itself might have caused parts of the phantom to be more compressed than other parts so the strain patterns are not perfectly symmetric. Images of the brachial artery, however, show that heterogeneity of the elastic medium surrounding the vessel produces an asymmetric strain pattern. Notice that if the frame with the most expanded channel were used as the reference for computing the strain image sequence, the gray-scale polarity of the strain image would reverse such that bright regions would become dark and dark regions bright. If a frame anywhere else during the pulse cycle were used as the reference, though the amount of decorrelation may be lowered, the polarity of the strain patterns would shift during the pulse cycle.

The phantom and brachial artery strain images suggest that regions with pulsatile blood flow can be mistaken for hard or soft targets when imaging with external compression. However, the strain patterns are characteristically different, which aids discrimination. Similarly Bilgen [1998] found that strain patterns surrounding targets with circular cross sectional areas reveal information about the out-of-plane dimension for imaging with external stimuli.

1.4.2. Spatio-Temporal Strain Variations across an Expanding Fluid Channel

Spatially, the largest displacement occurs at the channel wall, at $r = D/2$ in Eq. 1.1, and is reduced in proportion to the distance from the wall. We illustrate in Fig. 1.10 the displacement and strain that are measured using echo cross correlation along the beam axis and through the center of the channel. The left column explains the effects when the expansion is small or the correlation window is large relative to the diameter of the channel. The right column explains the effects for larger expansions and smaller correlation window lengths. Recall that strain is determined from displacements estimated over a correlation window. Pixels in a strain image correspond to movement of the correlation window to different locations.

When the correlation window, represented by the line segment "I" is placed outside the channel (region ***I*** at top left in Fig. 1.10a), we find the displacement averaged over the echo segment. Displacement in homogeneous viscoelastic media varies smoothly over space, so echo decorrelation will be minimal as long as the strain over the correlation window dimension is small, less than a one percent. As the correlation window enters the low scattering fluid channel (region ***II*** in Fig. 1.10a), displacement estimates are dominated by echoes at the channel wall, so the displacement plateaus at a peak. When the correlation window spans the channel to include echoes from both sides (region ***III*** in Fig. 1.10a), the average displacement falls rapidly to zero if the channel expands symmetrically. When the correlation window is positioned below the channel, as in regions ***IV*** and ***V*** in Fig. 1.10a, we measure the same displacement profile except in the opposite direction. Computing the spatial derivative we then find the strain. The simulated strain pattern in Fig. 1.10a suggests there should be a bright and dark region

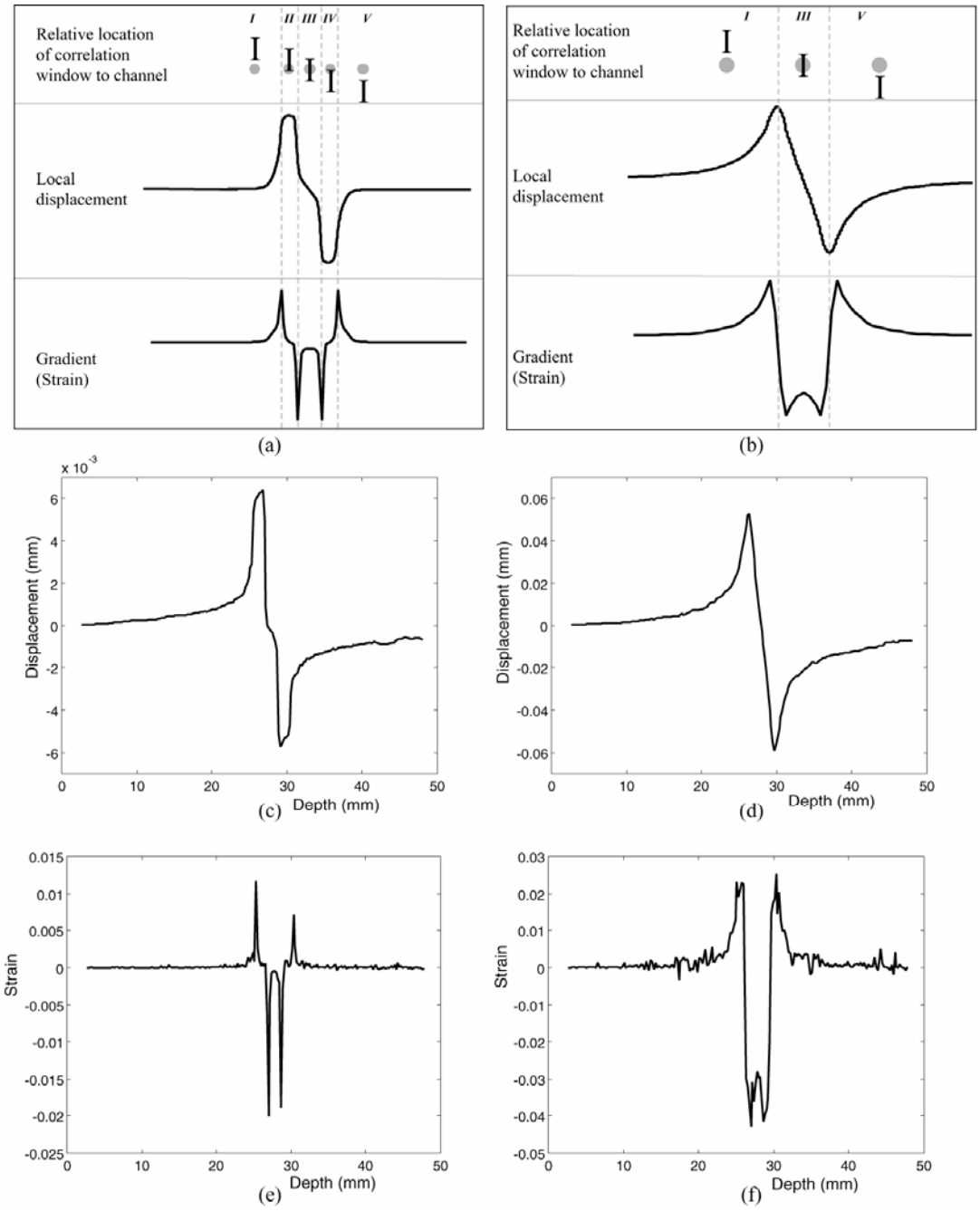

Fig. 1.10. Displacement and strain estimations are affected by the extent of channel expansion and the size of the correlation window. The left column (a, c, e) shows the effects when the expansion is small or the correlation window is large; the right column (b, d, f) shows the effects when the expansion is large or the correlation window is small (see text). (a) and (b) are the expected shapes (not drawn to scale) of local displacement and strain profiles along the center axial line at the channel. (c) and (e) are real displacement and strain estimates corresponding to the center axial line in Fig. 1.3a. (d) and (f) are real displacement and strain estimates corresponding to the center axial line in Fig. 1.3c.

centered at both walls of the channel. This is precisely what we observed in the images of Fig. 1.3. We plot one line of displacement and strain measurements from the phantom data of Fig. 1.3a in Figs. 1.10 c and 1.10e to show it is very similar to that predicted in Fig. 1.10a.

If the extent of the channel expansion is large or the correlation window is small, then we observe the responses illustrated in Fig. 1.10b. This is essentially a blurred version of the effects seen in Fig. 1.10a. Regions ***II*** and ***IV*** disappear due to the rapid drop in correlation between the reference frame and the displaced frame as the window shifts. Plotting a line of displacement and strain data taken from the image in Fig. 1.3c and plotting them in Figs. 1.10d and 1.10f, we again see that measured patterns are similar to those predicted. In summary, the dynamic strain patterns from our simple tissue-like pulsed-flow phantom are easily interpreted in terms of the interaction between object motion the imaging system properties, and the estimation procedure.

1.4.3. Relationships among Vascular Pressure, Elasticity and Strain

Studies have shown that vascular diameter varies proportionally with arterial pressure in elastic vessels [Summa 1978]. The phantom data presented in this report suggests that local strain is also proportional to the relative pressure inside the channel. However, the constant of proportionality depends on the stiffness of the vessel and materials surrounding the vessel. Investigators have chosen numerous ways to express the relationship among these three quantities [Lehmann 1999]. One such expression is pressure-strain elastic modulus $E_p = \Delta P / \varepsilon_r$, where the strain is approximated as the

relative change in vessel diameter $\varepsilon_r \cong \Delta D / D_0$ that occurs in response to the change in pressure [Peterson et al. 1960]. If E_p is unknown but is constant over the physiological range of pressure variations ΔP, then the strain measured near the vessel wall can be used to estimate the local pressure variation. This is what we observed from the data in Figs. 1.4 and 1.5. Measuring peak systolic and end-diastolic pressures with the sphygmomanometer while imaging the brachial artery may enable us to relate strain to relative pressure as in Figs. 1.4 and 1.5. These data should be acquired synchronously to detect any phase lag between the pressure and deformation pulses, which is likely because of the viscous response of blood vessels. Measurement of vascular elasticity is the subject of a future study.

1.5. CONCLUSIONS

Time sequences of strain images are very sensitive to internal deformations such as those caused by pulsatile arterial flow, as shown by a simple phantom study using a clinical imaging system. Displacements of order 10 μm and strains as small as 0.01 were quickly estimated in regions of area 0.7 x 0.8 mm^2 about a 1.3-mm-diameter flow channel. The strain patterns are very different from those generated using external stimuli but are easily interpreted for the simple phantom geometry. These data suggest a potential role for real-time strain imaging in measuring relative pressure or vascular elasticity non-invasively.

CHAPTER 2

Vascular Elasticity from Regional Displacement Estimates

Abstract

An ultrasonic method for measuring elastic properties of blood vessels is described. A time sequence of displacement or strain images measured over the cardiac cycle describes the spatial and temporal patterns of deformation surrounding arteries. This information is combined with a mathematical model to estimate an elastic modulus. Simulations of ultrasonic echo data from deformed tissues are analyzed to define a signal processing approach. Measurements in flow phantoms, with and without vessel-simulating channel walls, provide a check of the accuracy and precision of elasticity measurements. Finally, preliminary results in human volunteers are compared with measurements from the literature. We find that the technique is very sensitive to displacements and has potential in automatically segmenting the vessel lumen. It also provides an alternative method for measuring the elastic modulus of soft homogeneous materials.

Keywords: brachial artery, displacement, phantom, stiffness index, strain imaging ultrasound.

2.1 INTRODUCTION

An essential function of healthy vasculature is the storage of mechanical energy between cardiac pulses. Elastic arteries reduce the mean arterial pressure necessary to maintain constant perfusion. Advancing age and disease stiffen vessel walls and increase wall thickness and vessel diameter, often producing systemic hypertension that damages organ tissues. In vivo measurements of vascular elasticity can help explain the sources of hypertension and guide treatment strategies.

The mechanical properties of arteries are determined by the material content and microstructure of the vessel wall and surrounding medium. Large arteries have three layers containing collagen, elastin, and smooth muscle cells [Fung 1993, Kawasaki et al. 1987]. Muscle cells influence dynamic vascular properties but affect static mechanical properties very little [Wolinsky and Glagov 1964]. Most data in the literature describes the vessel's response to static loads. The highly flexible elastin fibers (0.3 MPa stiffness) distribute forces uniformly over the lumen surface. As the pulse pressure peaks and the lumen reaches maximum diameter, stress is progressively transferred to the inflexible collagen fibers (100 MPa stiffness).

The distribution of these materials in arteries varies with position of the vessel in the body; vessels located further from the heart tend to be less elastic, stiffer and more muscular. For example, in normotensive individuals, the aorta and carotids have highly elastic media layers and therefore lumen that expand nearly linearly with pressure. The

more distal brachial and femoral arteries have less elastic, more muscular media that respond nonlinearly by expanding more at low pressure than at high pressure.

Measurements of cardiac pulse wave velocities, lumen sizes and pressures yield common indices descriptive of vascular elasticity, and ultrasonic imaging is widely used for these studies [Imura et al. 1986, Reneman et al. 1986, Kawasaki et al. 1987, Hoeks et al. 1999, Eriksson et al. 2002, Rabben et al. 2002]. Most methods track vessel diameter changes during the cardiac cycle, measure systolic and diastolic pressures, and compute an index from the ratio that is based on a mathematical model of elasticity. Longitudinal deformation of the vessel is usually ignored. However it is difficult to track the low-contrast lumen-intima surface of the arterial wall particularly in older patients where the wall is loosely tethered to surrounding tissues. The high-contrast media-adventitia surface is easier to track but the lumen cannot be defined without a wall thickness measurement. We have proposed a method for measuring the deformation of tissues surrounding pulsatile vessels [Mai and Insana 2002], and are now combining that technique with mechanical models to estimate elastic moduli. Three levels of analysis of internal deformation are studied here. 1-D echo simulations offer completely known deformation but idealistic measurement conditions. Tissue measurements provide realistic conditions but are difficult to verify by independent means. Phantoms offer a middle ground. The combination of these three experimental results are analyzed to assess our ability to measure vascular elasticity in vivo.

2.2 METHODS

2.2.1 Theory

We first examine two approaches to mathematical modeling of the mechanical behavior of blood vessels under static loads; one is a rigorous model of a simplified linear-elastic tube and the other is an empirical model based on laboratory measurements of blood vessels.

Linear-Elastic Media.

Volterra and Gaines [1971] derive constitutive equations for a hollow channel of uniform linear-elastic material that is subjected to a static transmural pressure. Although blood vessels are complex multi-layered structures, this single-layer model serves to predict properties of simple tissue-like flow phantoms with well defined flow geometry and material properties, enabling the assessment of ultrasonic measurement reliability under experimental conditions.

The elasticity of the flexible flow channel material is summarized by Young's modulus, *E*. It is a thick, straight, cylindrical tube of length ℓ positioned perpendicular to the *z*-axis. Under initial equilibrium, the cylindrical channel has inner and outer radii r_1 and r_2, with wall thickness $h = r_2 - r_1$ (Fig. 2.1) [Saada 1974, de Korte et al. 1997]. Uniform pressures p_1 and p_2 are then applied to the inside and outside of the channel. The channel changes in size according to *E* and in response to the pressures. The extramural pressure p_2 can represent a reactive stress from the materials surrounding the finite-thickness channel as the channel expands. Thus p_2 may depend on the mechanical properties of materials outside the channel wall.

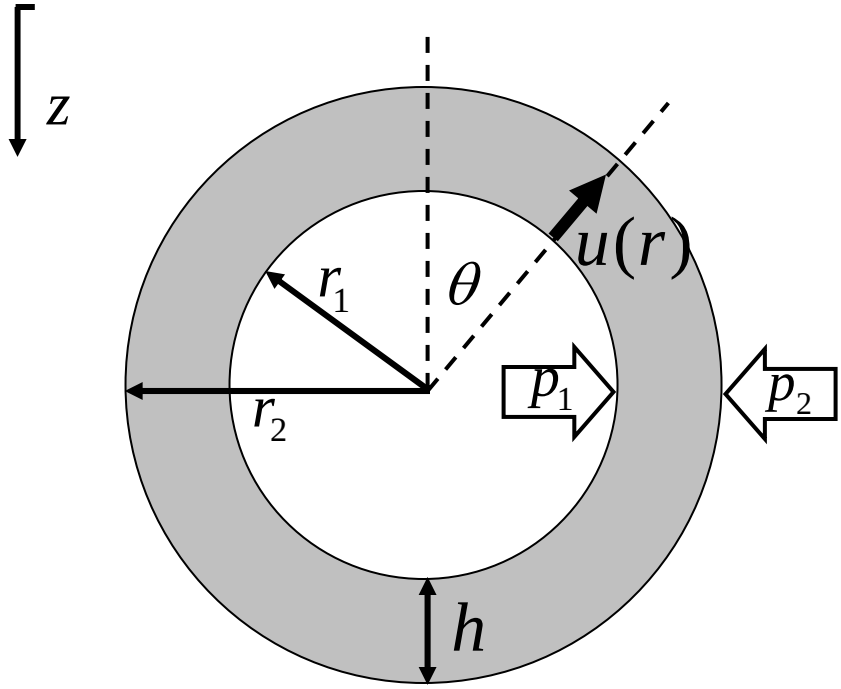

Fig. 2.1. The channel is assumed to be thick-walled cylinder, with initial inner and outer radii r_1 and r_2, wall thickness $h = r_2 - r_1$. Uniform pressures p_1 and p_2 are then applied to the inside and outside of the channel. $u(r)$ is the radial displacement of the wall at r distance away from the center. Depth z is the distance away from the transducer. θ is the angle between the direction of $u(r)$ and the axial line.

Stress components in cylindrical coordinates are $\sigma_r, \sigma_\theta,$ and σ_z. Geometric symmetry and material uniformity permit the reasonable assumption that σ_r and σ_θ are independent of θ, and the shear stress $\tau_{r\theta} = 0$. The displacements in polar coordinates corresponding to $\sigma_r, \sigma_\theta,$ and σ_z are $u, v,$ and w. Angle independent stresses imply a zero angular displacement, $v = 0$. The vessel is assumed to be tethered to the surrounding medium preventing movement along the z-axis; consequently, $w = 0$ and we have a two-dimensional, plane-strain problem.

For these conditions and at radial position $r_1 \le r \le r_2$, the relationships among strains, stresses, displacements, and position are [Volterra and Gaines 1971]

$$\begin{aligned} \varepsilon_r &= \frac{du}{dr} = \frac{1}{E}\left[\sigma_r - \upsilon(\sigma_\theta - \sigma_z)\right] \\ \varepsilon_\theta &= \frac{u}{r} = \frac{1}{E}\left[\sigma_\theta - \upsilon(\sigma_r - \sigma_z)\right] \\ \varepsilon_z &= 0 = \frac{1}{E}\left[\sigma_z - \upsilon(\sigma_r - \sigma_\theta)\right], \end{aligned} \tag{2.1}$$

where υ is Poisson's ratio of the wall material. Because of the cylindrical geometry, the angular strain ε_θ is nonzero even though the angular displacement v is zero.

Volterra and Gaines found the cylindrical components of stress from the Airy stress function in a lengthy derivation. Assuming the boundary conditions $\sigma_r(r_1) = p_1$ and $\sigma_r(r_2) = p_2$, and rearranging the last line of Eq. 2.1 to eliminate σ_z from the first two equations, we find the following relationships between pressure and stress:

$$\begin{aligned} \sigma_r &= \frac{r_1^2 r_2^2 (p_2 - p_1)}{r_2^2 - r_1^2}\frac{1}{r^2} + \frac{r_1^2 p_1 - r_2^2 p_2}{r_2^2 - r_1^2} \\ \sigma_\theta &= -\frac{r_1^2 r_2^2 (p_2 - p_1)}{r_2^2 - r_1^2}\frac{1}{r^2} + \frac{r_1^2 p_1 - r_2^2 p_2}{r_2^2 - r_1^2} \\ \sigma_z &= \frac{2\upsilon(r_1^2 p_1 - r_2^2 p_2)}{r_2^2 - r_1^2} \quad . \end{aligned} \tag{2.2}$$

Assume incompressibility $\upsilon = 0.5$ for physiological pressures. Defining the transmural pressure $P = p_1 - p_2$, where $p_1 \ge p_2$, we can combine Eqs. 2.1 and 2.2 to find the elastic modulus of the wall in terms of experimentally measurable quantities:

$$E = \frac{3P}{2ru(r)}\frac{r_1^2 r_2^2}{r_2^2 - r_1^2} \qquad r \ge r_1 \ . \tag{2.3}$$

Eq. 2.3 is used in the Results section below to estimate *E*, the elastic modulus of the latex wall in the flow phantom. The expression for a wall-less flow channel, i.e., a cylindrical hole in the gelatin phantom where $r_2 >> r_1$, is just

$$E_g = \lim_{r_2 \to \infty} E = \frac{3Pr_1^2}{2ru(r)} \qquad r \geq r_1 \ , \tag{2.4}$$

where E_g is the derived Young's modulus of the gelatin. These equations are derived for Hookean solids under static-force conditions; both are reasonable assumptions when *u*, p_1, p_2 are small.

Eq. 2.3 can be related to the pressure-strain elastic modulus, $E_p = p_1/(u/r_0)$, found throughout the literature [Peterson et al. 1960, Lehmann 1999] by assuming a thin walled vessel, $h/r_1 << 1$, and $r_0 = (r_1 + r_2)/2$ to find

$$E = 3r_0E_p/4h. \tag{2.5}$$

Eq. 2.5 links our phantom measurements to arterial elasticity indices found in the literature, whereas Eqs 2.3 and 2.4 enable comparison of Young's modulus estimates of the phantom from independent ultrasonic and mechanical measurements, as shown below. E_p ignores the dependence of elastic modulus on vessel diameter and wall thickness, yet is useful in measurement situations where accurate measurements of *h* and r_0 are unavailable. A result identical to Eq. 2.5 using a pulse-wave velocity measurement is illustrated in Bergel [1964] and Lehmann [1999]. These summarize the basic equations for linear-elastic vascular media.

Nonlinear-Elastic Media.

An elastic material is considered linear if the elastic modulus is constant at all applied pressures or stresses. In the pressure range of our experiments, gelatin phantom materials are isotropic, linear and elastic. However, biological tissues often exhibit nonlinear properties under normal physiological conditions due to a complex internal structure. Tanaka and Fung [1974] have shown that the tensile stress and the modulus do not always have a linear relationship in tensile tests of the artery segments. They also found that circumferential and longitudinal segments of arteries behave differently under tensile test. Within the physiological range, where elastic modulus increases proportionally with tension, however, a simple equation may be used to relate the tensile stress *T* along a circumferential segment to the stretch ratio $\lambda = 1 + \varepsilon_\theta$:

$$\frac{dT}{d\lambda} = \beta(T + \alpha) \ , \tag{2.6}$$

where β and α are constants. α is usually larger (less elastic) in peripheral arteries than in central arteries. Solving Eq. 2.6 for *T* shows an exponential relationship between tensile stress and the stretch ratio [Fung 1967],

$$T = (T_0 + \alpha)e^{\beta(\lambda - \lambda_0)} - \alpha \ , \tag{2.7}$$

where (T_0, λ_0) is a point on the stress-strain curve where Eq. 2.6 is valid. Taking the natural logarithm of Eq. 2.7 and rearranging factors gives

$$\beta = \frac{\ln[(T + \alpha)/(T_0 + \alpha)]}{\lambda - \lambda_0} \tag{2.8}$$

If we use σ_θ from in Eq. 2.2 to represent the tensile stress *T* in the vessel wall at $r = r_1$ and $p_1 >> p_2$, then $T = p_1(r_1^2 + r_2^2)/(r_2^2 - r_1^2)$ is proportional to luminal pressure. When

we apply this back into Eq. 2.8, and if $\alpha = 0$, $\lambda_0 = 1$, and the two internal pressure stages are at systole and diastole, then

$$\beta = \frac{\ln(P_s / P_d)}{u(r_1)/r_1} = \frac{\ln(P_s / P_d)}{(D_s - D_d)/D_d}. \tag{2.9}$$

This is the same stiffness index proposed by Kawasaki et al [1987], with D_s and D_d representing the artery diameter at systole and diastole respectively. Lehmann et al. [1999] found the stiffness index to be independent of pressure in normotensive subjects but not for patients at risk for vascular disease. Stress-strain curves for the brachial artery are nonlinear, consequently Eq. 2.4 does not apply. Instead, we report values of the stiffness index, Eq. 2.9, so that we can compare with published measurements. Notice that β is unitless and not directly comparable to an elastic modulus.

2.2.2 Algorithm

The displacement estimates are generated using a modified version of a strain imaging algorithm [Chaturvedi et al.1998a, Mai and Insana 2002]. Local displacements are determined by comparing pairs of RF data frames acquired at two different stages of deformation. Local strains can then be calculated as the rate of change in displacement field. The algorithm is designed to measure local displacements within the deformed object from 1-D or 2-D correlation lags determined at multiple spatial scales to improve the sensitivity. First, the global companding step, a course 2-D sum-absolute-difference correlation estimate, detects any overall strain or shift in the imaged region. This step may be skipped in phantom studies when the imaged region of interest is confined and no external stress is applied. Second, a local companding process measures 2-D

displacements at an intermediate-size spatial resolution and warp the echo fields accordingly. Finally, displacements are measured at the highest resolution by 1-D axial correlation of the companded echo frames, and then summed with the measurements from each stage. Limited by the ultrasound lateral resolution and the 1-D correlation step, only axial displacement $u_z = u\cos\theta$ and axial strain $\varepsilon_z = d(u\cos\theta)/dz$ are estimated (see Fig. 2.1). Contrary to the direction of depth *z*, upward (toward transducer) displacements are arbitrarily defined as positive; downward (away from transducer) displacements are negative. The transducer beam properties and the sizes of the companding and correlation windows determine the resolution and noise in the final strain and displacement images. 1.1mm x 1.0mm data windows searching in 2.2mm x 3.0mm regions are used for local companding. The size of the correlation windows used is 0.1 mm, except when specified.

2.2.3 Echo Simulation

To evaluate the displacement accuracy, the algorithms are first tested on a set of simulated ultrasound RF data along the diameters of channels. For simplicity, we model each 1-D object as an uncorrelated normal distribution of ultrasonic scatterers 51.7 mm in length. The object is then displaced from the center according to a rearranged Eq. 2.4: $u(r) = 3Pr_1^2/2rE$, where the displacement profile is proportional to 1/*r*. The maximal displacement magnitude, which can be arbitrarily designated in the simulation, thus occurs at the upper and lower channel walls $r = r_1, \theta = 0$ and π (part a in Figs. 2.2-2.5).

$$u_{\max} = \frac{3r_1P}{2E} \tag{2.10}$$

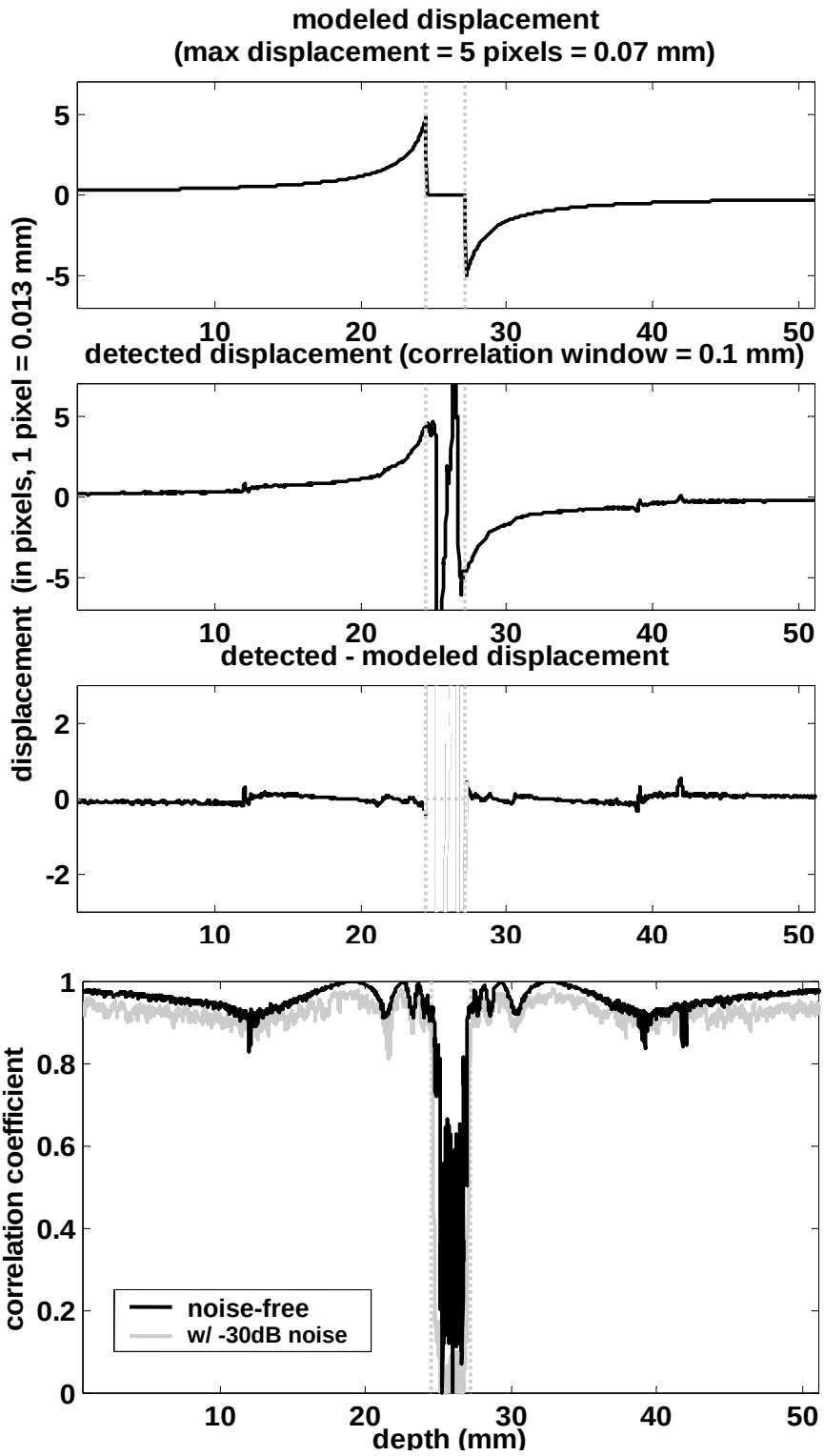

Fig. 2.2. (a) Simulated channel displacement, with u_{max}=5 pixels at the wall. (b) Detected displacement, processed with a small 8-pixel correlation window. (c) Difference between expected and estimated displacement. (d) Correlation coefficient between corresponding regions in pre- and post-displacement frames.

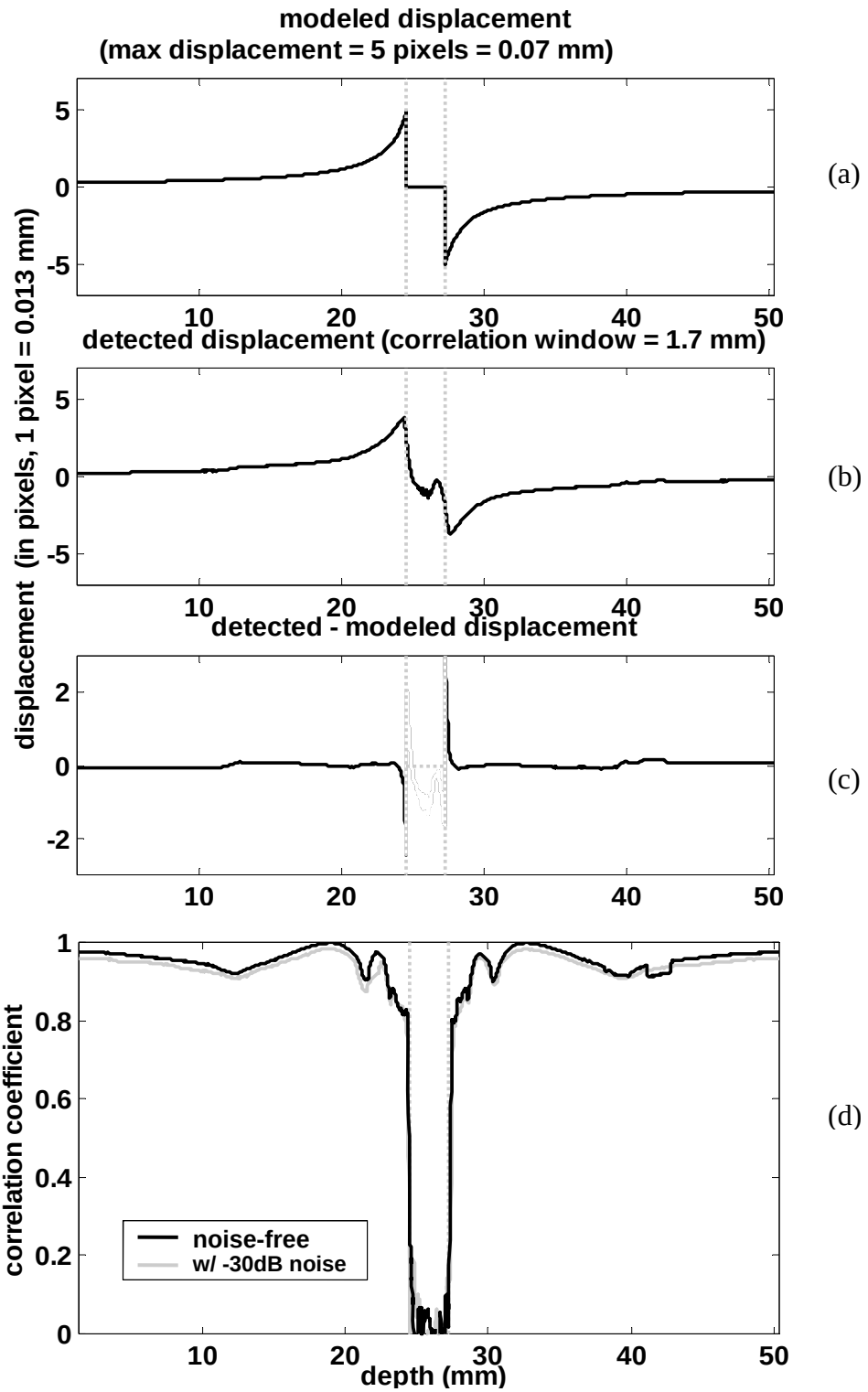

Fig. 2.3. (a) Simulated channel displacement, with u_{max}=5 pixels at the wall. (b) Detected displacement, processed with a larger 128-pixel correlation window. (c) Difference between expected and estimated displacement. (d) Correlation coefficient between corresponding regions in pre- and post-displacement

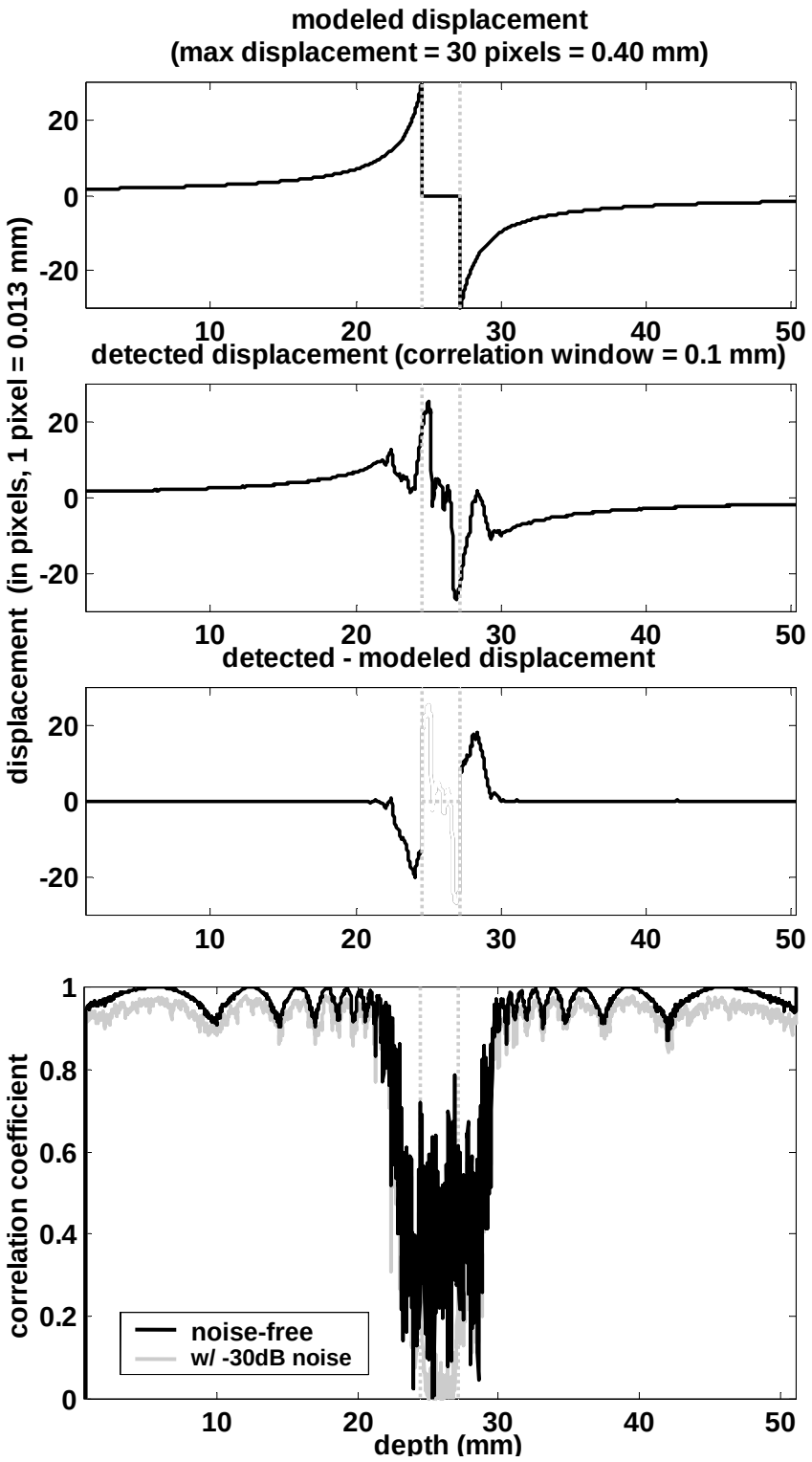

Fig. 2.4. (a) Simulated channel displacement, with u_{max}=30 pixels at the wall. (b) Detected displacement, processed with a small 8-pixel correlation window. (c) Difference between expected and estimated displacement. (d) Correlation coefficient between corresponding regions in pre- and post-displacement frames.

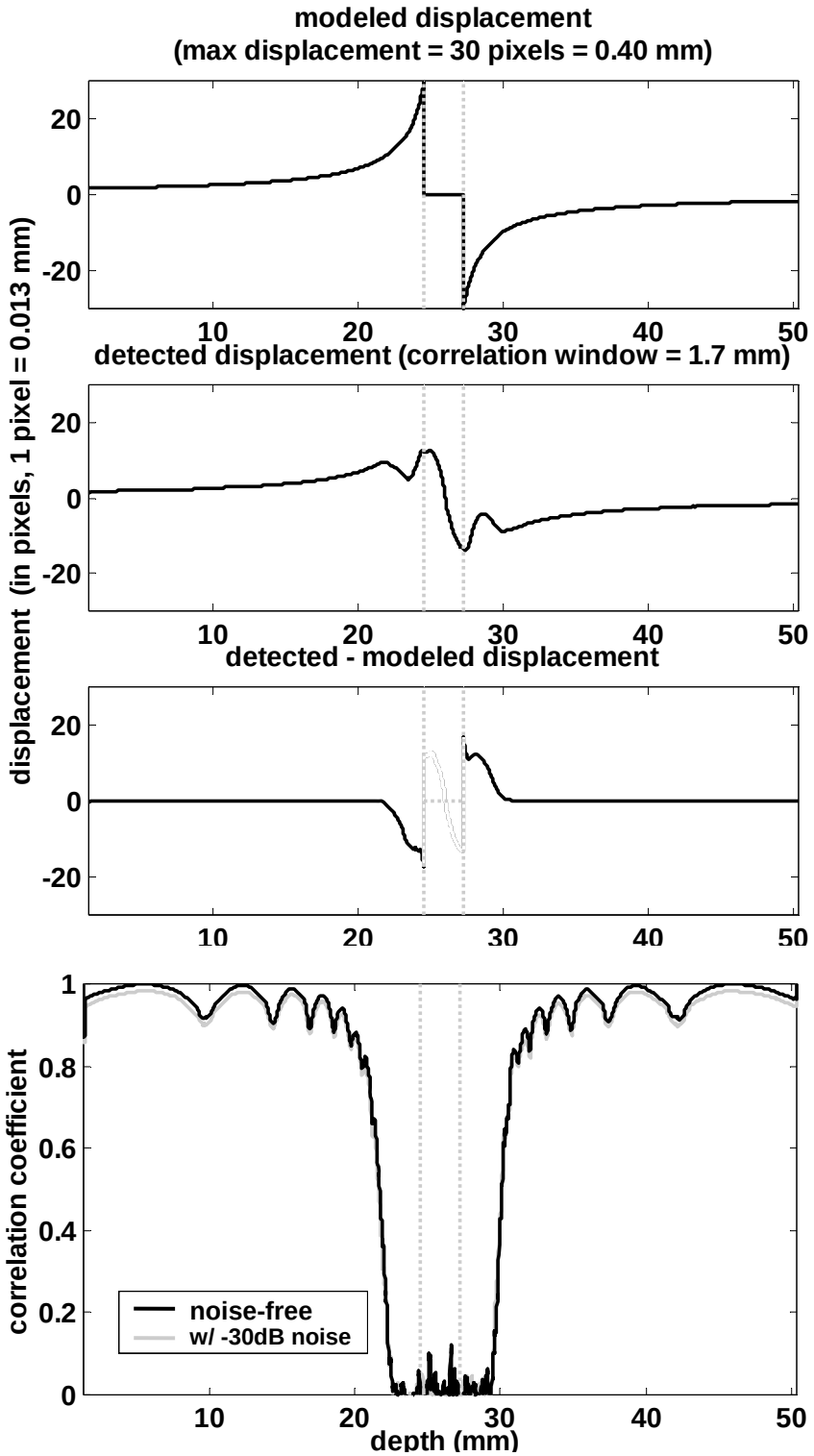

Fig. 2.5. (a) Simulated displacement at channel, with u_{max}=30 pixels at the wall. (b) Detected displacement, processed with a larger 128-pixel correlation window. (c) Difference between expected and estimated displacement. (d) Correlation coefficient between corresponding regions in pre- and post-displacement frames.

The center regions of both pre- and post-displacement objects are also replaced by SNR=30 dB Gaussian white noises that represent the fluid-filled channel, with the sizes of the regions differing by $2u_{max}$. The pre- and post-displacement object functions are then both convolved with the impulse-response function of the imaging system. The imaging transducer is a Gaussian-apodized, 7.2 MHz linear array with a Gaussian pulse of duration 0.1 μs [Insana 2000]. The simulated RF data are sampled at a rate of 57.6 Msample/s. Simulated system noise (SNR=30 dB) can then be added at this stage to each data. Both noise-free and noisy data are studied. For each measurement, a set of 312 independent waveforms is simulated.

Two different correlation window sizes are used to illustrate the effect of varying window size: a small 0.1mm (8 pixels) window and a larger 1.7mm (128 pixels) window. By comparing the known object displacement with the displacement estimated from the echo data, we are able to access accuracy and precision under ideal conditions.

2.2.4 Data Acquisition

The ultrasound data are acquired at 15 fps with a Siemens Elegra system using a 7.5 MHz linear array transmitting 7.2 MHz broadband pulses. The field of view is 38.5 mm wide and 51.71 mm deep. The echo data are acquired at 36 MHz, then demodulated and downsampled by a factor of 2.5, and stored as I/Q data for later transfer to a PC. The I/Q are then re-modulated and interpolated to 57.6 MHz RF data for off-line processing. Though we study independent axial lines in the simulation for simplicity of movement, the displacement estimations in phantom and in vivo studies are still similar. To minimize partial volume effects, we assume the vessel deforms only radially, and we

make measurement in the cross-sectional view. Long axis views are complicated by the weak elevational focusing of the linear array, and thus avoided.

2.2.5 Phantom Studies

Two ultrasonic flow phantoms, one with a wall-less channel and the other walled, were constructed. The bulk material of both phantoms is a congealed matrix of animal-hide gelatin in which a fine graphite powder is randomly suspended (83.93% distilled water, 7.72% n-propanol, 5.04% animal-hide gelatin powder (275 bloom), 0.05% formaldehyde, and 3.26% graphite powder). Construction details of this standard phantom material have been well described in past literature [Madsen et al. 1978, Hall et al 1997, Mai and Insana 2002]. The attenuation coefficient of the phantom material was found to be 2.92 dB/cm and the speed of sound was 1567 m/s when measured in distilled water at 21^{o}C and 7.5 MHz. Young's modulus E of the hydrogel was measured and found to be 7.4 kPa during the span of this study. We used an indentation test on the phantom surface following the method of Kargel et al. [2001]. Each phantom contains a hollow cylindrical flow channel of 3.175-mm diameter at the center of the gel block. Phantom I (Fig. 2.6a) has a wall-less channel that is produced by casting and removing a brass rod into the gelatin. Phantom II (Fig. 2.7a) has a straight segment of rubber tubing (70-mm long, inner diameter r_1 =3.175 mm, 0.794-mm wall-thickness h = 0.794 mm, Hygenic Hytone natural rubber latex tubing) embedded during construction. Acrylic cylinders of 75-mm diameter and 50-mm height confine the sides of the phantoms and act as anchors for the rigid plastic inlets and outlets to the channels. The top and bottom surfaces of the phantom are covered by thin plastic films that allow easy contact for transducer without confining the expansion of the phantom.

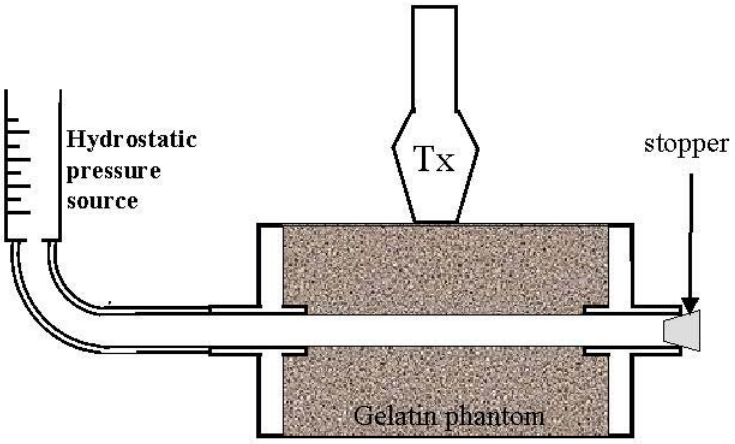

(a)

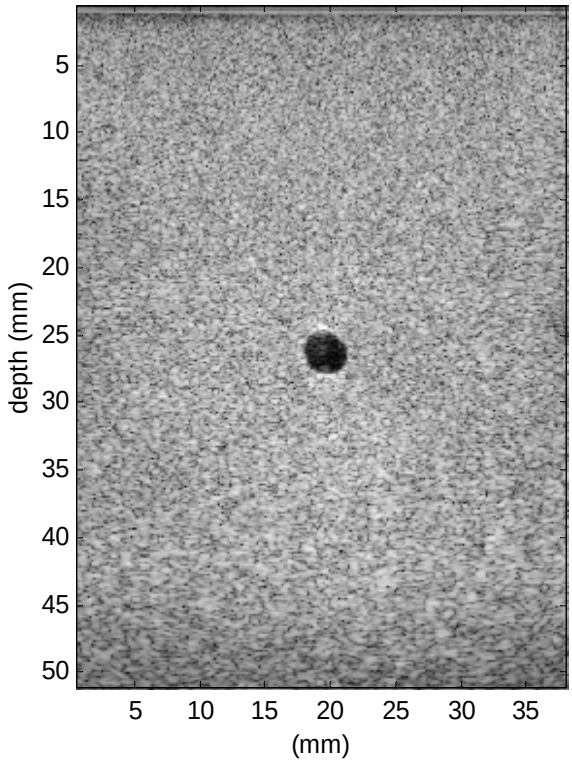

(b)

Fig. 2.6. (a) Setup of the wall-less channel phantom. (b) A sample B-mode image of the cross-section of the phantom.

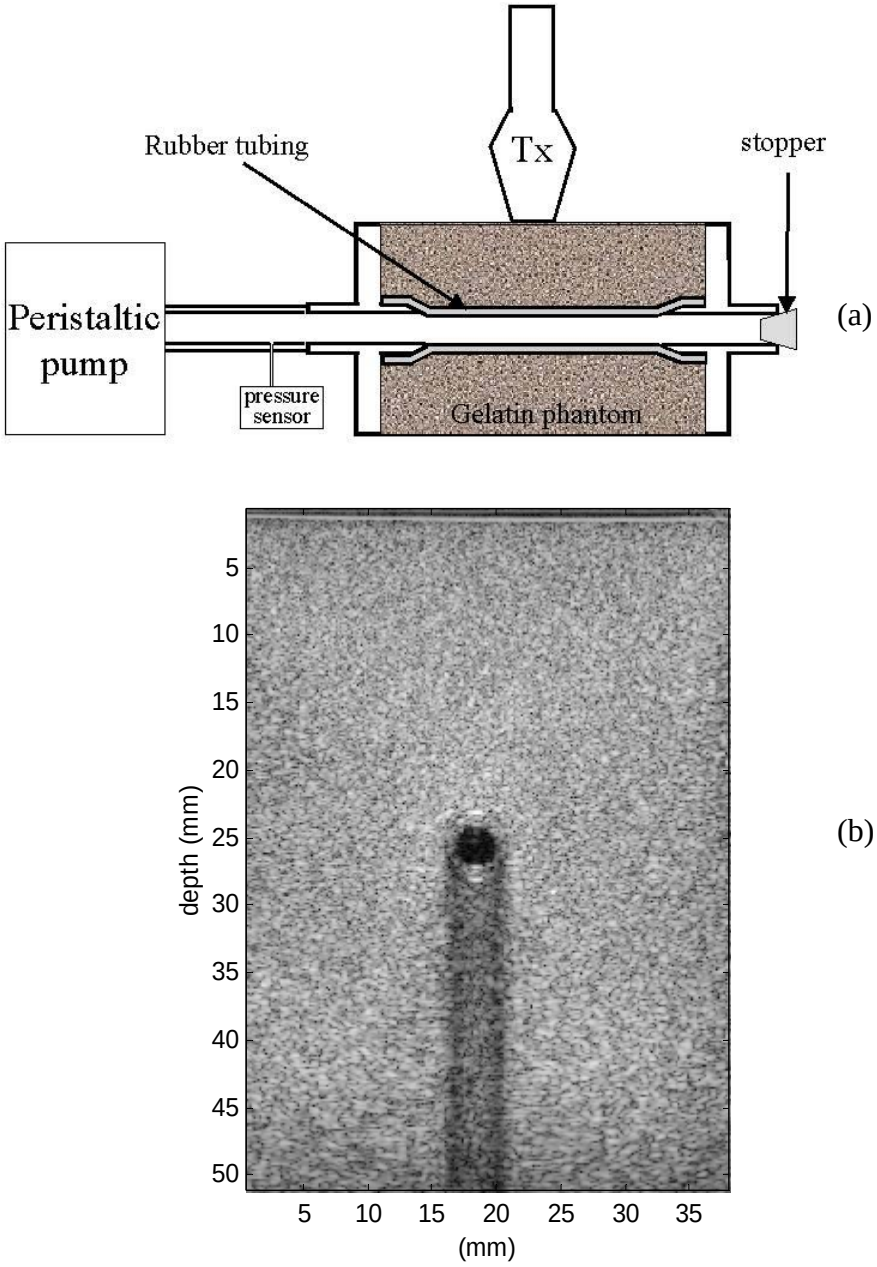

Fig. 2.7. (a) Setup of the walled channel phantom. (b) A sample B-mode image of the cross-section of the phantom, with shadow trailing the rubber tubing.

Hydrostatic Pressure in Wall-less Phantom

Though pulsatile flow can be easily produced in the phantom by connecting it to a peristaltic pump, hydrostatic pressure was applied to the channel in a controlled environment to measure channel-wall expansion u as a function of pressure P. The hydrostatic pressure is generated by connecting one end of the channel to a variable-height water column while sealing off the other end (Fig. 2.6a). The "zero pressure" water height was established by letting water move freely through the unsealed ends of the channel when the phantom was completely submerged in water. The echo frame acquired at this "zero pressure" was used as reference frame for generating displacement estimates. After sealing off the outlet of the channel, water was then added to the column at 1-cm increments to a maximum height of 15 cm, which converts to a pressure of 11.07-mmHg. Echo data of the same imaging plane is acquired at each pressure stage. Fig. 2.6b is a sample B-mode image of the cross-section of the phantom channel, after conversion from the RF echo data that we use for processing. As is common in tissue imaging, there are artifacts (reverberation and beam distortion) and decorrelated echoes (out-of-imaging-plane flow inside channel). Consequently, we can assume SNR for displacement is zero inside the channel where there is no useful information.

Increasing Pressure in Walled Phantom

Prior to data acquisition, the embedded rubber tubing was first filled with water for two days to minimize air trapped in the rubber, thus reducing the attenuation of the wall. Since the rubber material is much stiffer than the phantom gelatin, detectable expansion of the channel cannot be created with the mere increase in hydrostatic pressure

in the water column. Therefore, the expansion of the walled channel is created by continuously pumping water to one end of the tubing with a peristaltic pump while completely sealing off the other end (Fig. 2.7a). Though water volume increases inside the channel, there is essentially no flow. The channel gradually increases in diameter while the echo data of its cross-section is continuously recorded at 15fps. The pressure variation inside the channel was also monitored during the time of image acquisition with a medical pressure transducer system (Medex LogiCal pressure transducer, Puritan-Bennett Co. PB240 patient monitor). The echo data acquired at the onset of pressure change is used as reference frame to calculate the displacement estimates. The B-mode image of the cross-section of the phantom is shown in Fig. 2.7b, with a shadow trailing the tubing evident in figure. Though Eqs. 2.1-2.4 are derived for static conditions, we are assuming elastic theories can still be used here under quasi-static conditions where the change in pressure is small and applied slowly.

2.2.6 In Vivo Brachial Artery

The brachial artery cross-sectional images are acquired from the underside of the right arms of subjects in sitting position. The imaged region is near the upper third of the arm. The weight of the arm is supported by slanted adjustable plates that holds the transducer, thus creating a flat and flush surface around the region of transducer contact (Fig. 2.8a). An imaging plane is picked so that a clear contrast between the vessel and the surrounding tissue can be seen on the B-mode display (Fig. 2.8b). Subjects hold their breaths and are refrained from movement during data acquisitions. We acquired echo data from several consecutive cardiac cycles at 15 fps. The frame with the smallest

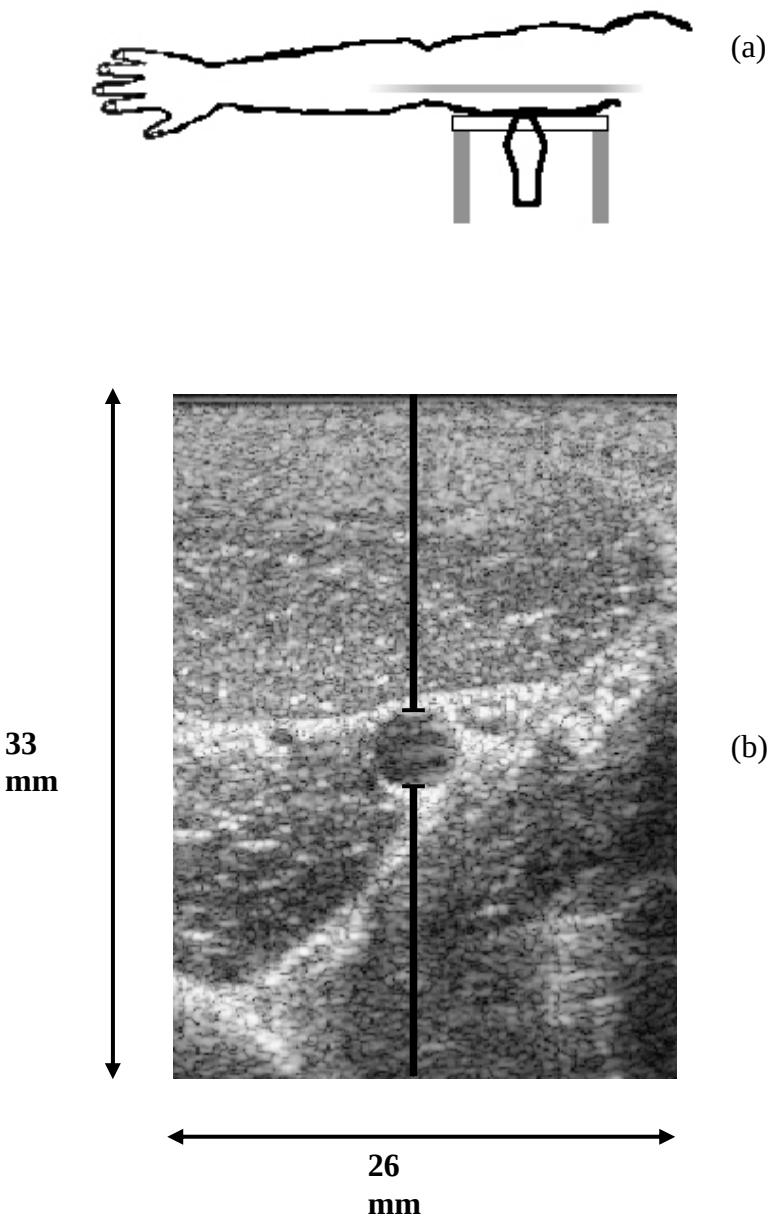

Fig. 2.8. (a) Setup of the in-vivo brachial artery imaging. (b) A sample B-mode image of the cross-section of the brachial artery.

arterial diameter, corresponding to end diastole, is the reference frame for processing. Besides using the general algorithms with the same parameters to calculate the displacements, an extra step of global companding with larger search windows may be applied beforehand to account for the overall shift in imaged regions. Systolic and diastolic arterial pressures are obtained with a sphygmomanometer at the right arms of the subjects after the acquisition of ultrasound data.

2.3 RESULTS AND DISCUSSION

2.3.1 Simulation

Fig. 2.2a is the modeled displacement along the channel diameter, where the edge of the simulated channel wall is displaced outwardly by 5 pixels (0.07 mm). The displacement decreases inversely proportional to the distance from the center of the channel as suggested by Eq. 2.3. The vertical dotted lines near the center of the plots indicate the locations of the channel walls. Fig. 2.2b is the detected displacement as a function of depth, processed with the small 0.1-mm correlation window and averaged over 312 noiseless echoes. Fig. 2.2c is the difference between the expected and the estimated displacements.

We can easily see from Fig. 2.2 that there is a large error inside the lumen of the channel. This is expected because the noise in the channel is uncorrelated between data frames. There is an under-estimation of displacement near the channel interface that extends into the outer scattering media a distance that depends on the pulse length and the correlation window length. Noisy simulations with an echo SNR=30dB are also studied,

but the displacement results are almost identical to that of noise-free situations and thus not shown in figures.

Correlation coefficients (ρ) were computed between pre- and post-displacement echo signals as a function of depth. These functions are shown in part d of Figs. 2.2-2.5. Instead of directly comparing regions at the same depth, the correlation coefficient $\rho(RF_{pre}(z), RF_{post}(z-\delta))$ is calculated between region in the pre-displacement echo data and its "corresponding" region (shifted by the amount of estimated displacement δ) in the post-displacement. Rounding is also necessary to determine the integer pixel indices for shifting since quadratic interpolation is used in the correlation step to estimate the fractional displacement δ. The correlation coefficient is used to partially explain the displacement errors. For example, Figs. 2.2-2.5 suggest the general results that displacement estimation is possible only when ρ is larger than 0.8, and the lowest errors are found for ρ larger than 0.88. Note that this ρ does not indicate whether a correct displacement can be estimated at a certain location prior to processing, but rather it indicates reliability of estimates and helps us decide if a feature is an artifact.

The correlation plots in black are for noise-free situations and the plots in gray are for noisy RF data (SNR=30 dB). Noise seems to reduce the correlation coefficient at all depths, whereas the noise-free correlation coefficient approaches one at many points. As expected, the correlation coefficient plummets inside the simulated channel, where the echo SNR=0.

Evident in part d of Figs. 2.2-2.5, the correlation plots exhibit an oscillation on both sides of the channel. The oscillation is caused by the numerical rounding of displacements δ into discrete pixel indices during calculation of correlation coefficient. Six local maxima are observed on each side of the channel in Fig. 2.2d, corresponding to the correctly identified six discrete levels of indexed displacement (zero to five). Since the strain is higher (displacement's rate of change is faster) near the channel, the width of each lobe gets smaller closer to the channel.

If we compare Fig. 2.2c and 2.2d where the correlation window size is 8 pixels, we can see that the correlation coefficients are all above 0.88 for accurate estimation outside the channel. However, if we look at Fig. 2.4 where the highest modeled displacement at channel wall is 30 pixels, we can see that inaccurate displacement estimates occur well outside of the channel. It appears that when the correlation coefficient drops below around 0.88, displacement estimates are no longer reliable. Of course, this lower limit of 0.88 is only valid for correlation window size of 8 pixels. With correlation window of 128 pixels, where spatial resolution is reduced, displacement estimates are accurate for correlation coefficients as low as 0.8 (Fig. 2.5). While idealistic, these echo simulation offer some guidance on deciding whether displacement estimates from phantom measurements are meaningful. Also note that in the correlation coefficient plot for the modeled 30-pixel displacement, the number of local maxima on each side of the channel is much less than the expected 30, since the discrete levels of correctly identified pixel displacement are much less than 30.

Though the correlation coefficient necessary for an accurate displacement is lower for a larger correlation window at a more evenly strained region, a smaller correlation window is needed to calculate the correct displacement at a highly strained (fast-changing displacement) region to avoid averaging and under-estimation. For this reason, most of the following phantom studies are processed with the small correlation window of 8 pixels (0.1 mm) at the 1-D correlation step.

2.3.2 Phantom Studies

For uniform radial expansion of the circular channel, the lateral center of the channel is located automatically by finding the axial line with the highest displacement magnitude. This is done by first locating the pixel with highest displacement magnitude for each lateral line at all depths. Then the median of these lateral locations is used as the lateral center for the whole data set. Median instead of mean is used to avoid large displacement errors. If we had prior knowledge of the axial location of the channel and if the frame with the smallest channel size was used as reference, the lateral center may be more accurately assessed by locating the axial line with highest positive displacements above the channel and lowest negative displacements below the channel, instead of searching for the maximum displacement magnitudes. The accuracy of the lateral channel center is also limited by the lateral resolution of the ultrasound system, since the RF data is not interpolated in the lateral direction. This also may not work well when there is only a small amount of displacement while the decorrelation inside the channel is much more significant.

Theoretically in an image where only the channel or vessel is expanding, the axial (vertical) center of the channel can be found at the midpoint between the locations with maximum upward and downward displacements. However, local maxima and minima in the displacement profile often exist within the lumen as a result of low echo SNR and decorrelation. Therefore the axial center may have to be determined as the midpoint between the first maximum and last minimum along the axial line of displacements, ignoring the local maxima and minima in between. Also, since the incorrect displacement estimation caused by decorrelation may be at a higher value than the maximum displacement at the channel wall, and the displacement along a single axial line can be noisy, the location of the axial center of the channel may be difficult to determine. This may be somewhat compensated by using the median axial center from several temporal frames or searching within limited range of displacement. Since all displacement and strain estimates are generated with the same reference frame, the estimated location of the channel center throughout the time series should all point to the same spot.

Due to limited sampling rate and beamwidth in the lateral direction, strain imaging techniques often compute only along the beam axis *z*. This is also the case with our algorithm, only axial displacement u_z is directly estimated. However, for a uniform radial expansion, the radial displacement *u* could be derived for anywhere in the echo field outside the channel, following the equation $u(r) = u_z(r,\theta)/\cos(\theta)$, where θ is the angle from the vertical axial line. Note that the axis *z* is a measure of depth away from

the transducer surface (Fig. 2.1), whereas *r* is the distance starting from the center of the channel, though both *r* and *z* may be aligned when θ=0 or θ=π.

Though $u_z(r,0)$ at the lateral center of the channel should be the representative of the radial displacement, $u(r)$, discrepancies can still occur due to system noise. We may minimize the errors by averaging over several angle-compensated *u*.

$$\bar{u}(r) = \frac{1}{N}\left[\sum_{\theta=-\phi}^{\phi}\frac{u_z(r,\theta)}{\cos(\theta)} + \sum_{\theta=\pi-\phi}^{\pi+\phi}\frac{u_z(r,\theta)}{\cos(\theta)}\right] \tag{2.11}$$

ϕ is limited to below π/6 to maintain a relatively high displacement SNR. N is the number of displacement estimates of u_z at the distance *r* that depends on digitization. Since N is small for small r, the estimates near the channel are still highly dependent on the data from the center axial line at θ=0 and θ=π. Displacements for regions above the channel $[-\phi,\phi]$ and below the channel $[\pi-\phi,\pi+\phi]$ can also be treated separately to maintain the signs in upward/downward displacements and detect possible non-uniform expansion.

Hydrostatic Pressure in Wall-less Phantom

Fig. 2.9a is the measured displacement profile u_z along the center axial line at the phantom channel under 3-cm H_2O pressure, processed with an 8-pixel correlation window. The vertical dotted lines near the center of these plots represent the location of the channel wall. Fig. 2.9b is the mean angle-compensated displacement $\bar{u}(r)$. We can see that Fig. 2.9a and 2.9b are very similar although 2.9a is noisier, showing that $u_z(r,0) = u(r)$. The broad gray dotted curves in Fig. 2.9b are *constant/r* curves showing

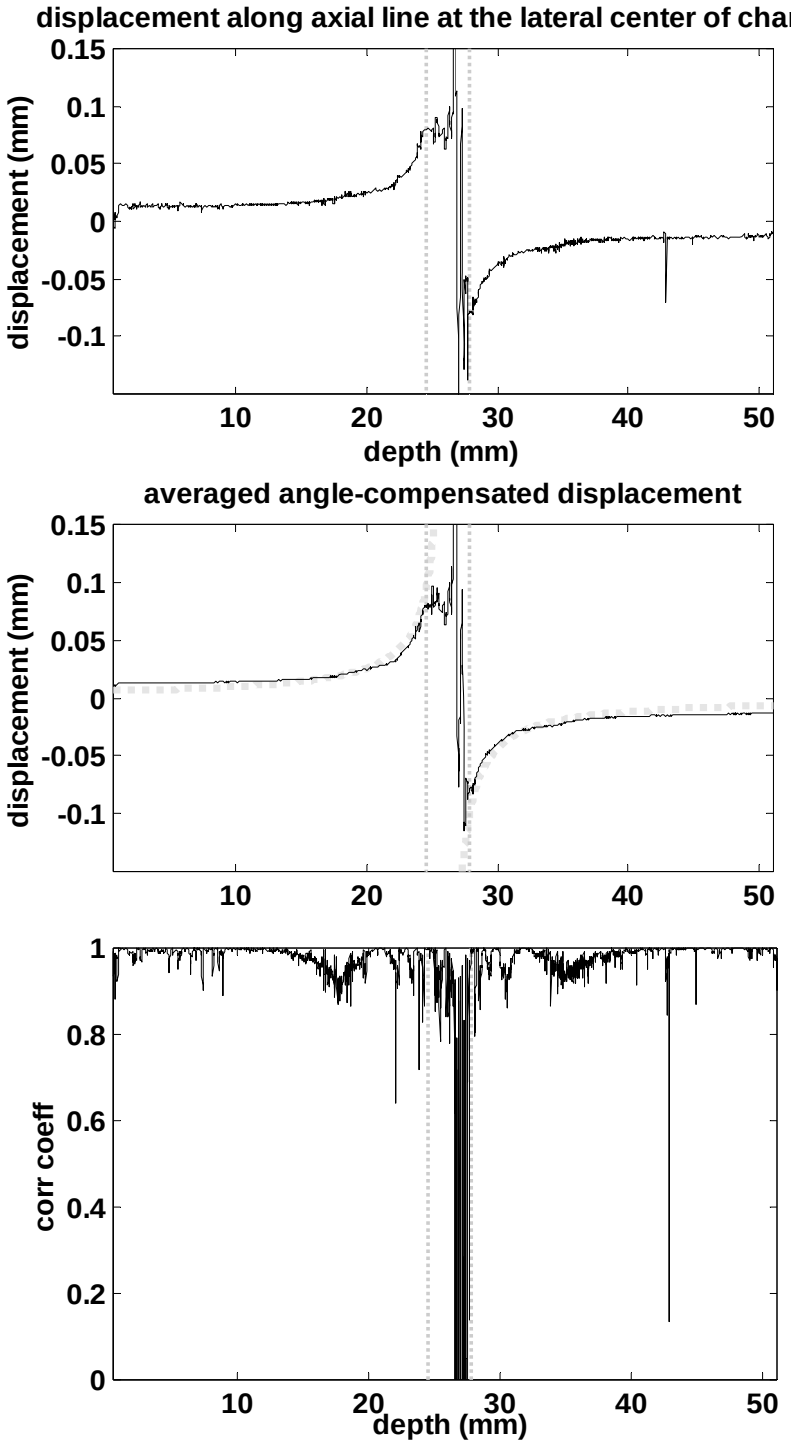

(a)

(b)

(c)

Fig. 2.9. (a) Axial displacement u_z along the center of the wall-less channel under 3-cm H_2O pressure. (b) Averaged angle-compensated displacement. (c) Correlation coefficient along the center axial line between corresponding regions in pre- and post-displacement frames from the wall-less phantom.

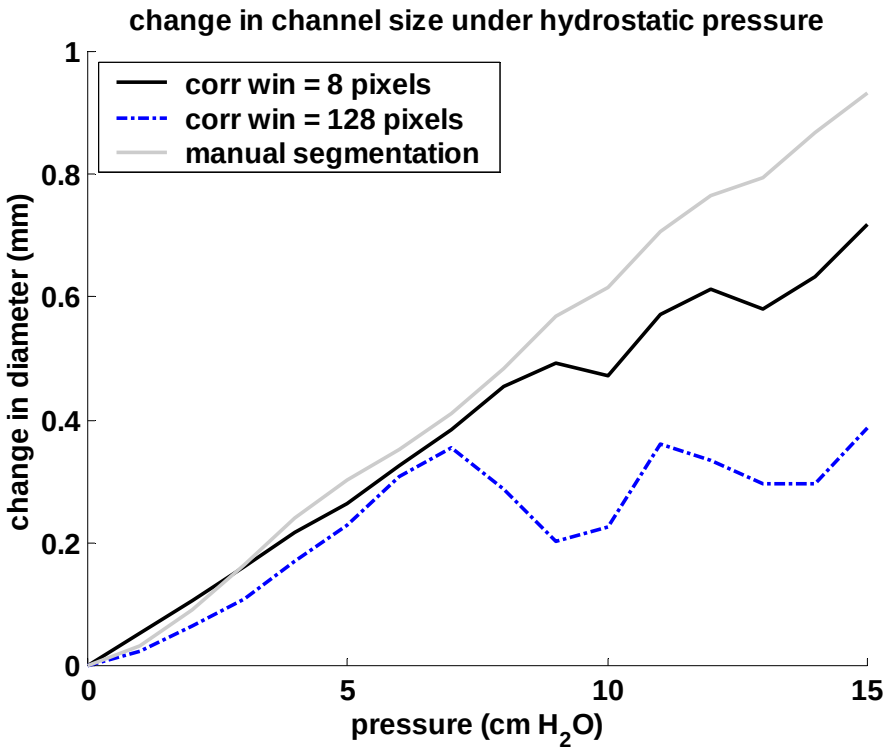

Fig. 2.10. The change in channel diameter is plotted as a function of applied hydrostatic pressure. The three plots represent the result of using 8-pixel (0.1-mm) correlation window displacement estimate, 128-pixel (1.7-mm) correlation window displacement estimate, and averaged B-mode manual segmentation. Displacement estimate's accuracy drops with increasing strain and displacement due to decorrelation and averaging.

that the displacement is indeed inversely proportional to distance *r* away from the center. Fig. 2.9c is the correlation coefficient along the depth of the same center axial line compared between pre- and post-expansion. With minor exceptions, correlation coefficients are mostly above 0.88 outside the flow channel, thus showing the estimations are valid. The measured phantom results are very similar to the simulation results, suggesting that simulations are predictive of the simple soft-tissue displacements.

Fig. 2.10 shows the change in channel size as a function of applied hydrostatic pressure. The three plots represent the result of using 8-pixel (0.1-mm) correlation

window, 128-pixel (1.7-mm) correlation window, and an averaged manual segmentation (ten trials of manual segmentation at each frame of B-mode image to estimate channel diameters). The smaller-window correlation seems to correspond to the manual segmentation better, while the larger-window correlation blurs the displacement more and gives an underestimation for fast-changing displacements (high strain). However, both sizes of correlation windows under-estimate displacement for larger expansion, as the amount of decorrelation and averaging increases. Nonetheless, observed systolic-diastolic change in brachial artery diameter is usually in the range of 0.2 mm to 0.3 mm [Kawasaki et al. 1987, Boutouyrie et al. 1994], which is still within our algorithm's tracking ability according to Fig. 2.10.

Using Eq. 2.4 and the corresponding pressures, we can calculate at any radial distance the elastic modulus E_g of the gelatin material that forms the channel. Fig. 2.11 shows the estimated elastic modulus as a function of distance from the channel wall ($r-r_1$). The pressure inside the channel for Fig. 2.11 is 3cm H_2O. The modulus is calculated by first averaging upward and downward displacements according to Eq. 2.11, then plugging it into Eq. 2.4. Though the elastic modulus of the material is expected to be constant through out the phantom, noises in the data and errors in displacement estimate can affect the measurement. We can see that the modulus remains between 8 and 4 kPa, though it does drop as it gets farther from the channel. We believe the underestimation of u at large distances is due to the fact that the phantom boundary is rigidly fixed and not infinitely thick and compressive as assumed in the equations. The ultrasound transducer and the rigid boundary act to increase p_2, creating a condition where P is lower than

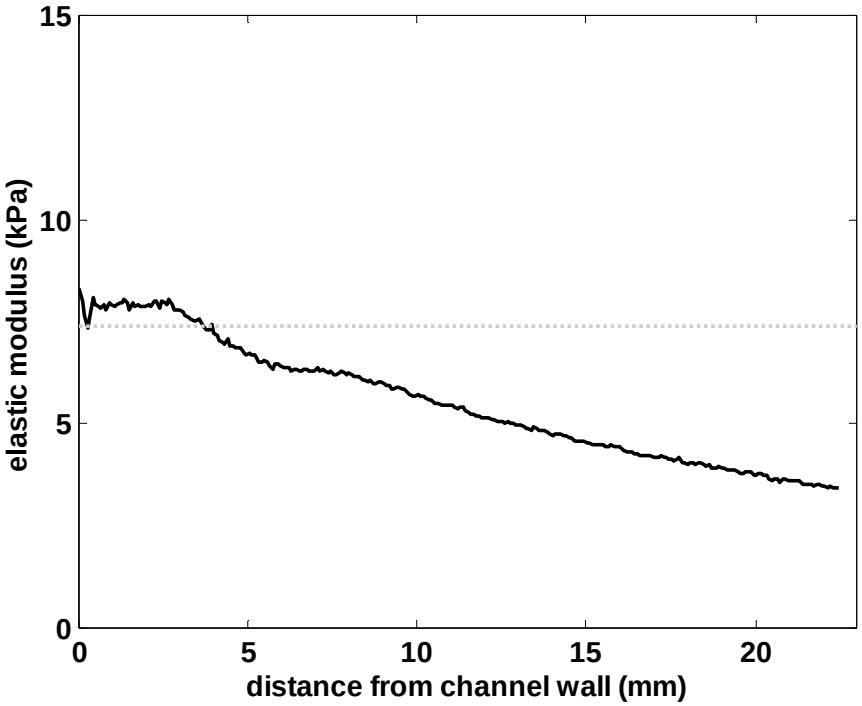

Fig. 2.11. The estimated elastic modulus is plotted as a function of distance from the channel wall (r-r_1) while the internal pressure is 3-cm H_2O. The modulus drops because the equation derived for infinite-thickness model no longer holds at the boundary.

expected, particularly near the boundary of the phantom. Eqs. 2.2-2.4 may not hold true for regions farther away from the channel. Incidentally, these regions are also at the very near or far fields of the transducer where lower echo resolution and SNR may contribute to incorrect estimates. Averaging the elastic moduli calculated within 5 mm of the phantom-lumen interface we find $E_g = 7.67 \pm 0.40$ kPa, in agreement with the 7.4 kPa measured from the indentation test (represented by the dotted gray line in Fig. 2.11).

Increasing Pressure in Walled Phantom

In Fig. 2.12a, the change $2\bar{u}(r_1)$ in tubing inner diameter is plotted for 60 consecutive frames, processed with an 8-pixel correlation window. The corresponding pressure inside the tubing is also shown in Fig. 2.12b. The notches on the pressure profile are caused by the rotating mechanics in the peristaltic pump, but their locations match the bumps in the tubing diameter plot. The change in tubing diameter appears to be linearly proportional to the change in pressure, at least within the range observed.

If we apply the measured displacement and pressure values to Eq. 2.3, we notice that p_2 is unavailable to us even though p_1 is measured with pressure transducer. We can actually derive p_2 by assuming it as a reactive stress from the gelatin acting on the latex tubing as the channel expands, similar to shrink fitting [Volterra and Gaines 1971]. In other words, p_2 becomes the pressure necessary to expand a wall-less gelatin channel with inner radius r_2 by the same amount as the gelatin-latex interface at r_2 has moved in the walled phantom. Thus $p_2 = 2E_g u(r_2)/3r_2$, where E_g is the elastic modulus of the gelatin material, $u(r_2)$ is the displacement of the outer wall of the latex tubing. We calculated p_2 for our setup and found that it is very small compared with p_1. Since the phantom is placed in ambient room pressure, the external pressure acting on the entire phantom is much smaller than that inside the channel. The known listed elastic modulus of the rubber material is also much higher than that of the gelatin. Therefore, We may even treat p_2 as negligible and it would not affect the equations much.

Plugging these data at $r = r_1$ into Eq. 2.3, we can evaluate the elastic modulus of the tubing at different frames, which is plotted in Fig. 2.12c. The averaged elastic

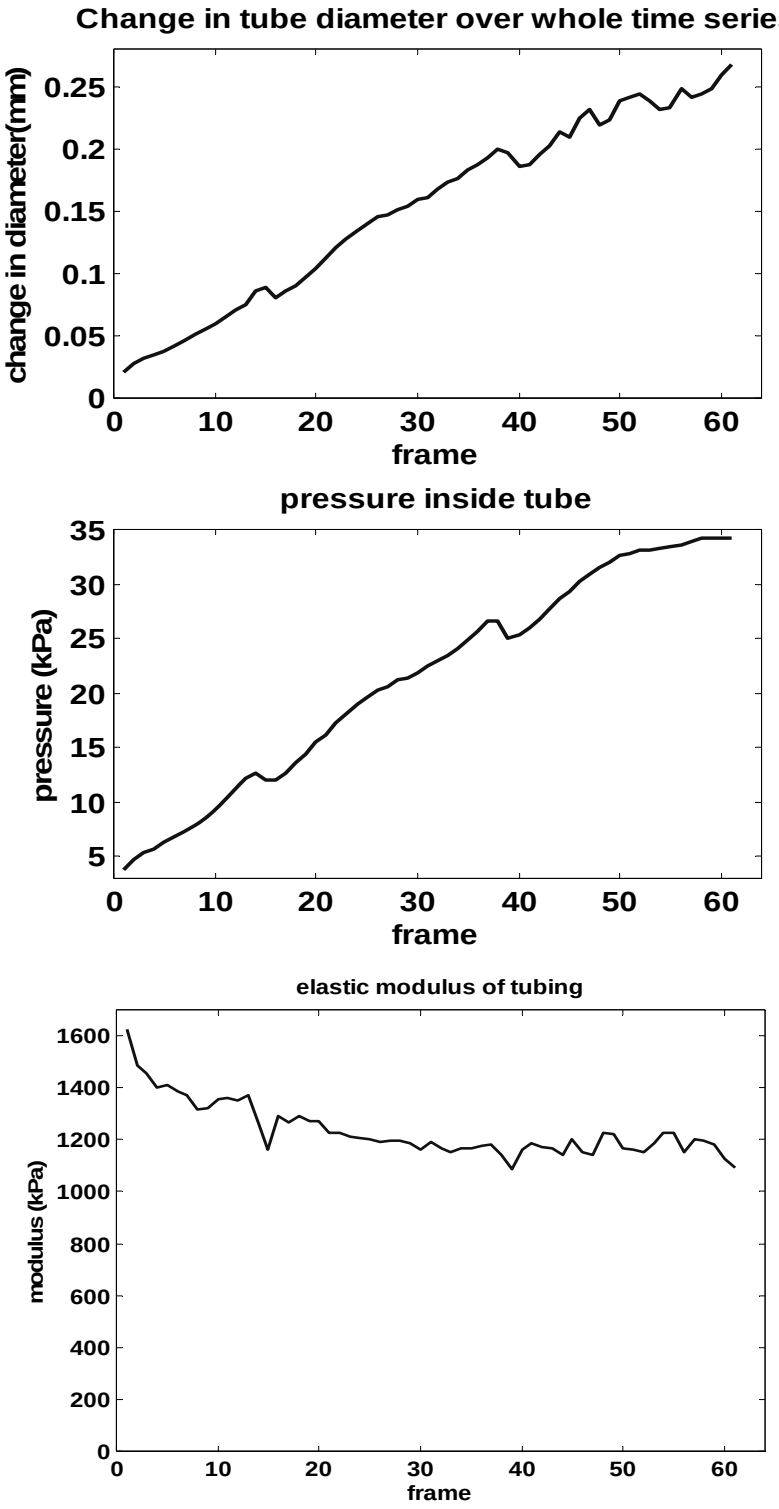

Fig. 2.12. (a) The estimated change in tubing inner diameter is plotted for 60 consecutive frames. (b) The corresponding pressure inside the tubing. (c) The elastic modulus of the tubing is calculated using the measured pressure and estimated displacement.

modulus of the tubing over the whole time series is 1230 kPa, which is actually about twice the mean modulus (655 kPa) listed by the manufacturer. Several factors could have contributed to this. First, the equations used usually describe a static condition, so the inertial and viscous components of the full constituitive equations are ignored in Eq. 2.3. Second, gravity, partially restrained boundary conditions, and finite-thickness of the material can all contribute to the non-symmetry of the phantom. Third, aging of rubber and initial stretched state of the tubing may also increase the modulus.

Also, the calculated modulus seems to decrease with increasing pressure, contradictory to conventional strain hardening [Bicerano 1996]. We may attribute this to the fact that an under-estimation in displacement at low-expansion is more likely to affect the modulus than a same error in larger expansion.

Lumen Segmentation in Longitudinal Views of Phantom Channels

Much of the arterial elasticity studies in past literatures have been performed on data of longitudinal view of arteries. This is at times favored due to the number of available axial lines for which similar displacement estimates can be calculated. But this approach encounters the difficulty of aligning the transducer to the center plane of a channel or artery, and relatively poor out-of-plane focusing of the transducer can also exacerbate the situation.

Our algorithm can be equally effective when applied to 2-D echo data of the longitudinal view of an expanding channel. Furthermore, one possible additional

application is the automatic detection of channel walls. Since the displacement estimates are calculated relative to the original locations in the frame with the smallest channel size, the intensity of each pixel in displacement image represents how much that very pixel has moved relative to the reference echo data frame. We also know that the highest displacement occurs at the channel wall, as it is the location under highest pressure. Therefore, the location of the pixel with the highest displacement should represent the location of the channel wall in the reference frame. Since we accurately follow the displacement of this pixel throughout the time series, we can find the exact location of the channel wall at all times by simply adding the amount of displacement to the reference wall location.

$$wall\_location(t) = location_{maxdisp} + disp(location_{maxdisp}, t)$$

A maximum upward motion should correspond to the proximal (upper) wall, whereas the largest downward motion indicates the location of the distal (lower) wall. By locating the proximal and distal walls for each axial line in the longitudinal view of a channel, the lumen then is automatically segmented. In Fig. 2.13a, the expanding wall-less channel under 4-cm H_2O internal pressure in a gelatin-graphite phantom is automatically detected and outlined. The phantom is the same wall-less phantom used in the cross-sectional view studies, placed under hydrostatic pressure from within the channel. Since the channel is expected to expand equally between axial lines, a 1-D median filter of 16 pixels is applied to the displacements along each row to reduce noise. A filter based on limiting the rate of change in displacement can also be applied to prevent mistaking decorrelation as the maximum displacement, since a feature of decorrelation is a large displacement gradient. However, in places where there is an overall axial shift instead of

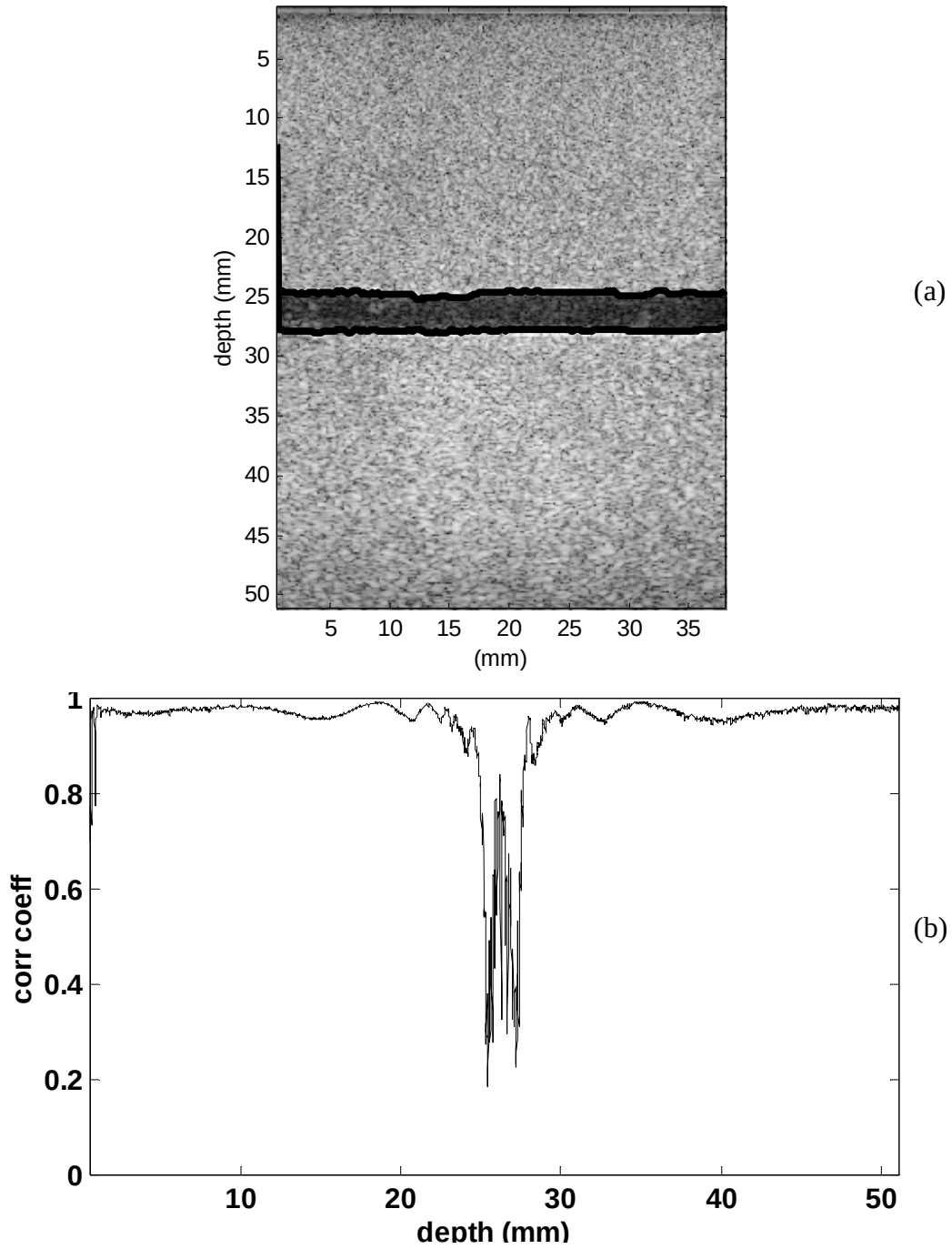

Fig. 2.13. (a) Channel wall can be automatically traced by locating the pixel with largest displacement at each axial line. The channel of a gelatin-graphite phantom under 4-cm H_2O pressure is automatically detected and outlined. (b)The averaged correlation coefficients over the axial lines of the longitudinal view of the phantom channel.

bi-directional expansion of the channel, such as in some arteries, it becomes very difficult to track the walls. Also, in cases where the level of expansion is very low compared with the noise level, the walls cannot be correctly located.

The plot in Fig. 2.13b is the averaged correlation coefficients over the axial lines of the longitudinal view of the phantom channel. This plot is analogous to the mean correlation coefficient plot in Fig. 2.2, but utilizes measurement data. This phantom data matches that of the simulation data very well.

2.3.3 In Vivo Brachial Artery

Fig. 2.14a is a sample 1-D RF data along the center of a brachial artery at diastole. The ultrasound transducer is positioned at depth 0 mm. The lumen of the brachial artery, which is marked between the dotted gray lines, can be easily recognized as the low amplitude region at the center of the plot. The non-zero signals inside the lumen are results of reflection of the anterior arterial wall and echoes from red blood cells. Fig. 2.14b shows the estimated displacement profile along the center of the brachial artery, processed with diastolic and systolic frames using 8-pixel correlation window. Fig. 2.14c is the averaged angle-compensated displacement profile. From Fig. 2.14c we can see that the location with the maximal downward displacement correspond fairly well to the location of the posterior wall. However, the anterior wall does not match with an easily identified maximal upward displacement. Though complete decorrelation is expected within the lumen, noisy but non-zero upward displacements are still observed there.

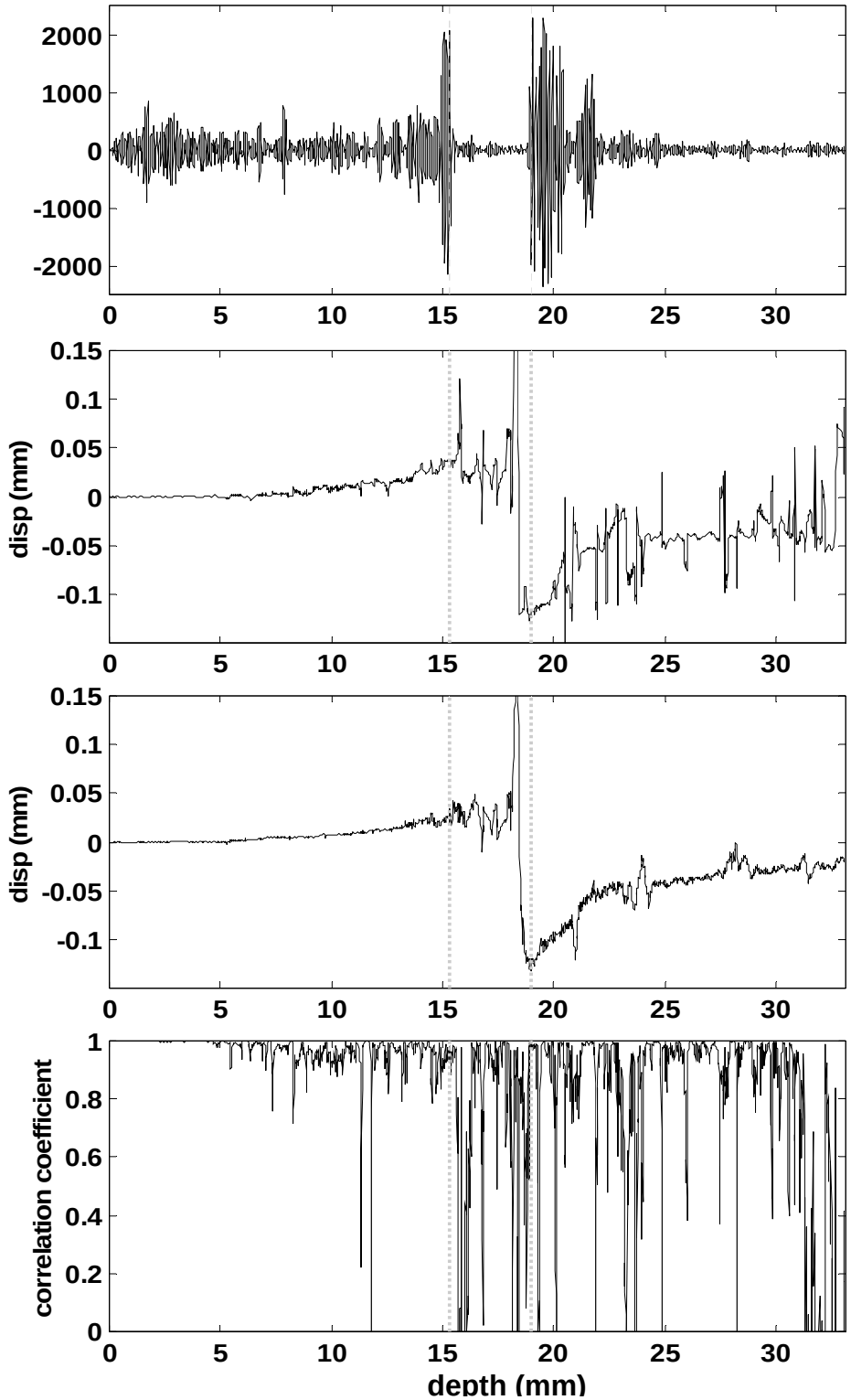

Fig. 2.14. (a) RF data at the brachial artery, with the gray dotted lines marking the lumen. (b) Axial displacement at the brachial artery between diastole and systole. (c) Averaged angle-compensated displacement. (d) Correlation coefficient of corresponding regions between diastolic and systolic frames.

These erroneous estimates can be easily mistaken as the displacement of the arterial wall. The displacement estimates also become noisier as the depth increases.

From Fig. 2.14bc we can see the displacements on the two sides of the artery are not symmetric. This suggests that there may be an overall shift in position, which might have been emphasized by the excessively high compression from the transducer surface.

Fig. 2.14d shows the correlation coefficient of displaced corresponding regions between diastolic and systolic frames. The luminal region has a lower correlation coefficient compared to regions outside. From the transducer surface to the proximal wall of the artery, the correlation coefficients are above 0.8 for the main parts, if not above 0.88. Also as expected, the regions farther away from the transducer have lower coefficients due decorrelation caused by out-of-plane motion and loss of resolution.

Table 2.1. Measured brachial artery parameters

	subject 1	subject 2	subject 3	subject 4
age (y)	25	27	27	24
P_s (mmHg)	135	128	120	118
P_d (mmHg)	80	73	75	61
D_d (mm)	3.64	4.26	4.15	4.44
D_s-D_d (mm)	0.16	0.13	0.053	0.11
β	11.9	18.4	36.8	26.6

Table 2.1 lists the measured brachial artery's parameters including stiffness indices for four male subjects. The change in artery diameter is calculated as the difference between the upward displacement at proximal wall and the downward

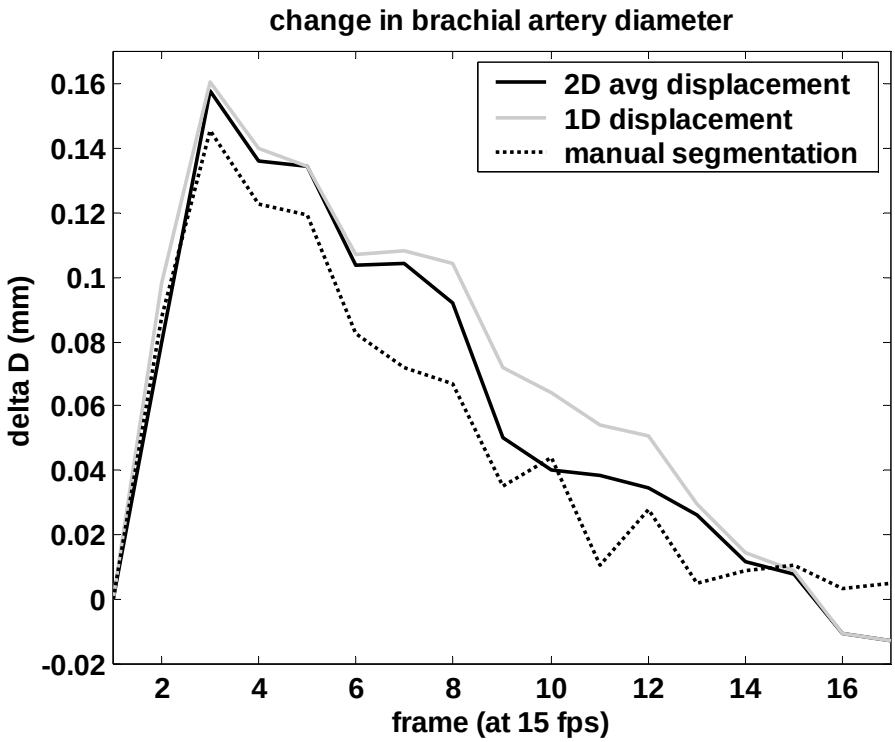

Fig. 2.15. The change in brachial artery diameter during one cardiac cycle for subject 1 is plotted, using displacement from center axial, averaged angle-compensated displacement, and B-mode manual segmentation.

displacement at distal wall, since downward displacements are treated as negative values. The change in brachial artery diameter during one cardiac cycle for subject 1 is plotted in Fig. 2.15, using displacement from center axial, averaged angle-compensated displacement, and manual segmentation of B-mode. Though the plot in Fig. 2.15 is comparable to normal brachial artery pressure profile [Remington and Wood 1956], and the measured pressure and diameter values from Table 1 are mostly within one standard deviation of the mean listed values in literatures [Kawasaki et al 1987, Boutouyrie et al. 1994], our calculated stiffness indices are much higher than those listed ($\beta = 8.68 \pm 3.79$) for the age group. The bias may be due to the high amount of compression applied to the arm by the transducer. Since the weight of the arm is sitting

on the transducer-embedded plate, it is creating an external stress on the artery, making it more difficult for the arterial pressure to expand the vessel. The nearby muscle tissues also exhibit increased elastic modulus under compression [Kargel 2001], creating stiffer boundaries around the artery. Unfortunately, since there is no way of telling how much stress was applied from the transducer by each subject, it is impossible to establish how the force applied affect the modulus calculated.

Though most of the time the expansion of the artery is assumed to be radially uniform, it may not be so. Lesion formation of the arterial wall or the presence of bone in the surrounding tissues may cause the artery to expand asymmetrically. Therefore, a single displacement profile from averaging over angle-compensated displacement may not be as representative of the diameter change as is in phantom studies. In addition to the difference in expansion pattern from that of phantom channel, arteries are more likely to exhibit an overall shift in location during the cardiac cycle due to the varying boundary condition and inhomogeneous tissues in the surrounding. Consequently it could be very difficult to select the center of the artery to calculate angle-compensated radial displacements. If the overall shift is in one of the axial direction, then the displacement of the wall in the opposite direction may appear much lower in amplitude and therefore cannot be tracked by locating the pixel with largest displacement. Also, although care was taken to ensure that the transducer is perpendicular to the arm, the transducer may still be placed at an oblique angle to the artery, causing the echo profile to be elliptical. For these reasons, it may not be a good idea to use the averaged angle-compensated radial displacement as an indication of the brachial artery's change in size as how it was used

for phantom. Nonetheless, independent axial displacement profiles of the cross section of artery can still assumed to be correct, similar to studies done on the longitudinal view of the artery. Also, the 2-D image of the displacement can still provide information on whether there's an overall shift of the artery and if there's any biased local displacement or expansion in surrounding regions.

There are other problems in displacement estimates of the brachial artery. In addition to the multiple layers in the arterial wall, there are connective tissues (fasciae) and fatty tissues surrounding the brachial artery, as seen in the B-mode image in Fig. 2.8b. These tissues exhibit different acoustic properties and are likely to create reverberations that are mistaken as artifacts within the lumen. During the systolic phase of the cardiac cycle while the arteries are expanded, the tissues surrounding the arteries may get compressed, causing the reverberated echoes to travel less distance between surfaces and thus making the artifacts of reverberation to appear closer to the transducer. As these artifacts shift closer to the transducer, they may have moved a longer distance than the arterial wall itself has actually displaced. As a result, it would be incorrect to locate the arterial wall by simply finding the pixel with the maximum displacement. However, if the location of the arterial is known in the reference frame, the displacement calculated for that location could still be treated as a valid estimation of the channel wall.

Another problem with *in vivo* imaging is the abundant sources of decorrelation. Any motion can cause out-of-plane motion, especially in regions far away from the transducer where any small rotation of the arm can move the reference imaging-plane out

of the beamwidth of the transducer. The tissue motions cause by breathing and unintentional muscle contractions may bring about global shift in the imaged region. The extent of the expansion of the artery may also be beyond the tracking ability of the algorithm, creating decorrelation where there is large amount of motion. The flow of blood may also cast shadow below the artery, besides having random RBC signals that effect decorrelation inside the lumen. The tissue's complex geometry and structure can all contribute to non-ideal acoustic and elastic properties, generating artifacts and noises that may eventually lead to incorrect displacement estimation.

2.4 CONCLUSION

From the simulations we can see that our algorithm is very sensitive to small displacements. From the controlled phantom studies, we see that the noise level in displacement estimates may be lowered by averaging over angle-compensated displacement profiles. The matched pressure readings and displacement estimates from an expanding channel can present an alternative way to measure the elastic modulus of a homogeneous material. The *constant/r* shape of the displacement profile also provides information on the locations of the walls of a channel so that the lumen may be tracked automatically. In the brachial artery imaging, though the valid vascular elasticity is somewhat limited by our acquisition setup, it is still able to track displacement fairly correctly. The next step in improving this study would definitely be alleviating the external applied stress thus reducing the variables in boundary conditions in both phantom and in vivo studies. An increased population for in vivo study may present a

more objective data. Measurements on smaller arteries can illustrate the effective of our algorithm, while tracking of larger and more elastic vessels may provide information more representative of vascular health.

APPENDIX

Strain Imaging with External Compression

The conventional strain image is usually generated by comparing the echo data from an object at pre-compression and post-compression. The source of compression is mostly external, often applied in the same direction of the ultrasound beam. Fig. A.1 illustrates the setup in which the cross-section of a stiff inclusion in phantom is imaged. The pre-compression echo data is acquired first at a static state. The transducer-embedded compressor plate then compresses the phantom uniformly from above. While two faces of the phantom are free to expand under compression, the two faces of the phantom that are parallel to the imaging plane are confined to prevent out-of-plane motion that can cause decorrelation. While holding the phantom at a desired amount of compression, the post-compression frame is acquired. We use the pre-compression frame as the reference for estimating displacements and strains so that any subsequent strain estimation may be mapped to the same reference.

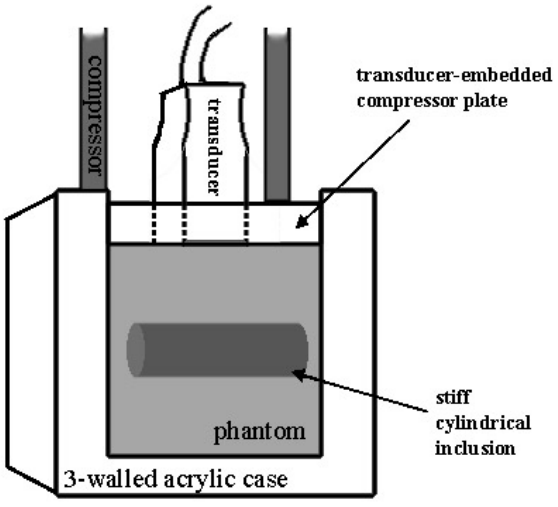

Fig. A.1. Illustration of the setup for strain imaging.

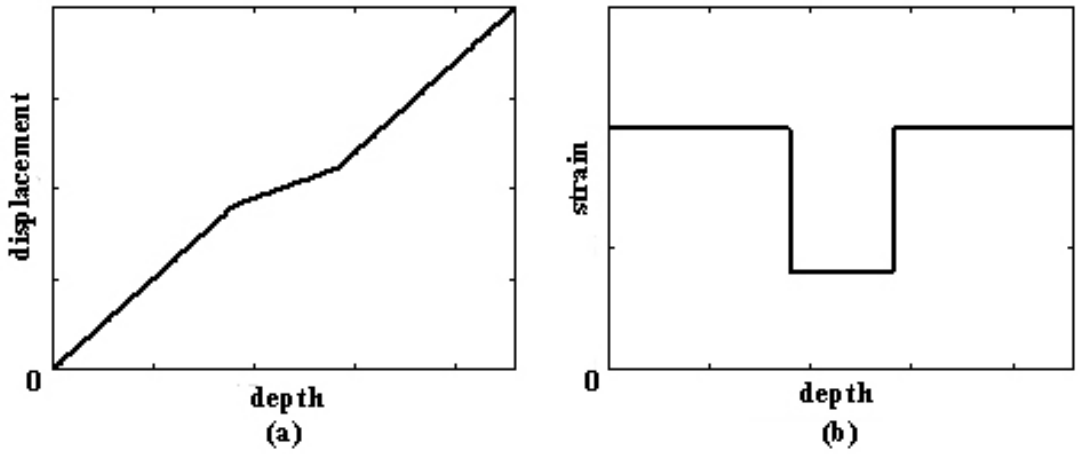

Fig. A.2. Illustration of compression-resulted displacement and strain plots of a stiffer region sandwiched by softer regions.

Under compression, the imaged region moves toward the transducer, with the farther region displaced the most (modeled in Fig. A.2a). Since softer material are more compressed (higher strain) than the stiffer regions, the rate of change in displacement varies along the depth (modeled in Fig. A.2b). A stiffer region appears darker in the strain images, with its neighboring softer regions under higher strain and appearing brighter. If the amount of external compression is increased, the elastic contrast between soft and stiff tissues would becomes more evident. However, decorrelation also increases with higher compression. A high elastic contrast may also be achieved by summing strain results from multiple small compression. The distribution of strains in the images is also dependent on the size of the compressor, boundary conditions, and the geometry of the inclusion.

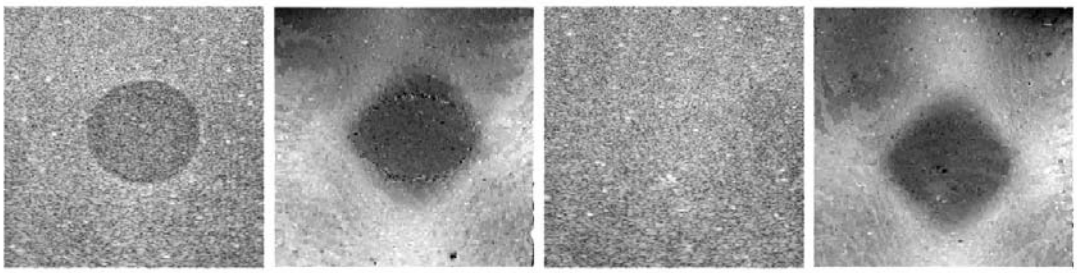

Fig. A. 3. B-mode (a, c) and strain (b, d) images for two tissue-like phantoms with 15 mm-diameter cylindrical inclusions, having an elastic modulus three times that of the background. Images (a, b) show the visible inclusion and (c, d) show an invisible inclusion.

Sample B-mode and corresponding strain images of a phantom similar to the one in Fig. A.1 are shown in Fig. A.3ab. The elastic modulus of the inclusion is roughly three times that of the background. An acoustically uniform stiff inclusion in phantom, undetectable in B-mode (Fig. A.3c), can be located with strain imaging (Fig. A.3d).

REFERENCES

Adler RS, Rubin JM, Bland PH, Carson PL. Quantitative tissue motion analysis of digitized M-mode images: gestational differences of fetal lung. Ultrasound Med Biol 1990;16:561-569.

Arndt JO, Klauske J, Mersch F. The diameter of the intact carotid artery in man and its change with pulse pressure. Pflügers Archiv 1968;301:230-240.

Bergel DH. Arterial viscoelasticity. In: Attinger EO. Pulsatile Blood Flow. London: McGraw-Hill, 1964:279-290.

Bicerano J. Prediction of Polymer Properties, 2nd ed., New York: Marcel Dekker, 1996.

Bilgen M, Insana MF. Elastostatics of a spherical inclusion in homogeneous biological media. Phys Med Biol 1998;43:1-20.

Boutouyrie P, Lacolley P, Laurent S, London GM, Safar ME. Intrinsic modifications of the brachial and radial arteries in hypertensive humans. Clin Invest Med 1994;17:97-106.

Céspedes I, Huang Y, Ophir J, Spratt S. Method for estimation of subsample time delays of digitized echo signals. Ultrasonic Imaging 1995;17:142-171.

Céspedes I, Ophir J, Ponnekanti H, Yazdi Y, Li X. Elastography: elasticity imaging using ultrasound with application to muscle and breast in vivo. Ultrasonic Imaging 1993;15:73-88.

Céspedes I, Ophir J. Reduction of image noise in elastography. Ultrasonic Imaging 1993;15:89-102.

Chaturvedi P, Insana MF, Hall TJ. 2-D companding for noise reduction in strain imaging. IEEE Trans Ultrason Ferroelect Freq Contr 1998a;45:179-191.

Chaturvedi P, Insana MF, Hall TJ. Testing the limitations of 2-D companding for strain imaging using phantoms. IEEE Trans Ultrason Ferroelect Freq Contr 1998b;45:1022-1031.

de Korte CL, Céspedes EI, van der Steen AFW, Lancée CT. Intravascular elasticity imaging using ultrasound: feasibility studies in phantoms. Ultrasound Med Biol 1997;23:735-746.

de Korte CL, van der Steen AFW, Céspedes EI, Pasterkamp G, Carlier SG, Mastik F, Schoneveld AH, Serruys PW, Bom N. Characterization of plaque components and vulnerability with intravascular ultrasound elastography. Phys Med Biol 2000;45:1465-1475.

Dickinson RJ, Hill CR. Measurement of soft tissue motion using correlation between A-scans. Ultrasound Med Biol 1982;8:263-271.

Eriksson A, Greiff E, Loupas T, Persson M, Pesque P. Arterial pulse wave velocity with tissue pulse Doppler imaging. Ultrasound Med Biol 2002;28:571-580.

Fung YC, Biomechanics: Mechanical Properties of Living Tissues, 2nd ed., New York: Springer-Verlag, 1993.

Fung YC. Elasticity of soft tissues in simple elongation. Am J Physiol, 1967;28:1532-1544.

Garra BS, Céspedes EI, Ophir J, Spratt SR, Zuurbier RA, Magnant CM, Pennanen MF. Elastography of breast lesions: initial clinical results. Radiology 1997;202:79-86.

Hall TJ, Bilgen M, Insana MF, Krouskop TA. Phantom materials for elastography. IEEE Trans Ultrason Ferroelect Freq Contr 1997;44:1355-1365.

Hoeks APG, Arts TGJ, Brands PJ, Reneman RS. Comparison of the performance of the RF cross correlation and Doppler autocorrelation technique to estimate the mean velocity o f simulated ultrasound signals. Ultrasound Med Bio 1993;19:727-740.

Hoeks APG, Brands PJ, Willigers JM, Reneman RS. Non-invasive measurement of mechanical properties of arteries in health and disease. Proc Instn Mech Engrs 1999;213:195-202.

Hoeks APG, Ruissen CJ, Hick P, Reneman RS. Transcutaneous detection of relative changes in artery diameter. Ultrasound Med Bio 1985;11:51-59.

Imura T, Yamamoto K, Kanamori K, Mikami T, Yasuda H. Non-invasive ultrasonic measurement of the elastic properties of the human abdominal aorta. Cardiovasc Res 1986;20:208-214.

Insana MF, Cook LT, Bilgen M, Chaturvedi P, Zhu Y. Maximum-likelihood approach to strain imaging using ultrasound. J. Acoust Soc Am 2000;107:1421-1434.

Insana MF, Myers KJ, Grossman, LW. In: Sonka M, Fitzpatrick JM, ed. Handbook of Medical Imaging: Volume 2. Medical Image Processing and Analysis. Washington: SPIE Press, 2000:515:565.

Kargel Ch, Trummer B, Plevnik G, Pellot-Barakat C, Mai JJ, Insana MF. Is Ultrasonic imaging a sensitive indicator of spatially varying elastic anisotropy? Proc IEEE Ultrason Symp 2001;2:1659-1662.

Kawasaki T, Sasayama S, Yagi S, Asakawa T, Hirai T. Non-invasive assessment of the age related changes in stiffness of major branches of human arteries. Cardiovasc Res 1987;21:678-687.

Lehmann ED. Terminology for the definition of arterial elastic properties. Path Biol 1999;47:656-664.

Levinson SF, Shinagawa M, Sato T. Sonoelastic determination of human skeletal muscle elasticity. J Biomech 1995;28:1145-1154.

Madsen EL, Zagzebski JA, Banjavic RA, Jutila RE. Tissue mimicking materials for ultrasound phantoms. Med Phys 1978;5:391-394.

Madsen EL, Zagzebski JA, Frank GR, Oil-in-gelatin dispersions for use in ultrasonically tissue-mimicking materials. Ultrason Med Biol 1982;8:277-287.

Mai JJ, Insana MF. Strain imaging of internal deformation. Ultrasound Med Bio (accepted 2002).

Ophir J, Céspedes I, Ponnekanti H, Yazdi Y, Li X. Elastography: a quantitative method for imaging the elasticity of biological tissues. Ultrasonic Imaging 1991;13:111-134.

Peterson LH, Jensen RE, Parnell J. Mechanical properties of arteries in vivo. Circ Res 1960;8:622-639.

Rabben SI, Bjærum S, Sørhus V, Torp H. Ultrasound-based vessel wall tracking: an auto-correlation technique with rf center frequency estimation. Ultrasound Med Biol 2002;28:507-517.

Remington JW, Wood EH. Formation of peripheral pulse contour in man. J App Physiol 1956;9:433-442.

Reneman RS, van Merode T, Hick P, Muytjens AMM, Hoeks APG. Age-related changes in carotid artery wall properties in men. Ultrasound Med Biol 1986;12: 465-471.

Rickey DW, Picot PA, Christopher DA, Fenster A. A wall-less vessel phantom for Doppler ultrasound studies. Ultrasound Med Biol 1995;21:1163-1176.

Saada AS. Elasticity: Theory and Applications. New York: Pergamon Press, 1974.

Salans AH, Katz LN, Graham GR, et al. A study of the central and peripheral arterial pressure pulse in man: correlation with simultaneously recorded electrokymograms. Circulation 1951;4:510-521.

Silver FH, Biological Materials: Structure, Mechanical Properties, and Modeling of Soft Tissues. New York: New York University Press, 1987.

Skovoroda AR, Emelianov SY, Lubinski MA, Sarvazyan AP, O'Donnell M. Theoretical analysis and verification of ultrasound displacement and strain imaging. IEEE Tans UFFC 1994;41:302-313.

Sonka M, Liang W, Lauer RM. Flow-mediated dilation in brachial arteries: computer analysis of ultrasound image sequences. CVD Prevention 1998;1:147-155.

Summa Y. Determination of the tangential elastic modulus of human arteries in vivo. In: Bauer RD, Busse R, ed. The arterial system: dynamics, control theory and regulation. Berlin; Heidelberg; New York: Springer-Verlag, 1978:95-100.

Tanaka TT, Fung YC. Elastic and inelastic properties of the canine aorta and their variation along the aortic tree. J Biomechan 1974;7:357-370.

Tristam M, Barbosa DC, Cosgrove DO, Nassiri DK, Bamber JC, Hill CR. Ultrasonic study of in vivo kinetic characteristics of human tissue. Ultrasound Med Biol 1986;12:927-937.

Varghese T, Ophir J, Céspedes I. Noise reduction in elastograms using temporal stretching with multicompression averaging. Ultrasound Med Biol 1996b;22:1043-1052.

Varghese T, Ophir J. Performance optimization in elastography: multicompression with temporal stretching. Ultrasonic Imaging 1996a;18:193-214.

Volterra E, Gaines JH. Advanced strength of materials. New Jersey, Prentice-Hall, 1971.

Wilson LS, Robinson DE. Ultrasonic measurement of small displacements and deformations of tissue. Ultrason Imaging 1982;4:71-82.

Wolinsky H, Glagov S. Structural basis for the static mechanical properties of the aortic media. Circ Res 1964;14:400-413.

Zagzebski JA, Madsen EL. Ultrasound phantoms – concepts and construction. In: Goldman LW, Fowlkes JB, ed. Medical CT & ultrasound: current technology and applications. Madison WI: Advanced Medical Publishing, 1995:121-142.

Zhang M, Zheng YP. Estimating the effective Young's modulus of soft tissues from indentation tests – nonlinear finite element analysis of effects of friction and large deformation. Med Eng Phys 1997;19:512-517.